

The STAR-MELT Python package[★] for emission line analysis of YSOs[†]

Justyn Campbell-White,¹ ‡ Aurora Sicilia-Aguilar,¹ Carlo F. Manara,²
Soko Matsumura,¹ Min Fang³, Antonio Frasca,⁴ and Veronica Roccatagliata^{5,6,7}

¹*SUPA, School of Science and Engineering, University of Dundee, Nethergate, Dundee DD1 4HN, U.K.*

²*European Southern Observatory, Karl-Schwarzschild-Strasse 2, 85748 Garching bei München, Germany*

³*Purple Mountain Observatory, Chinese Academy of Sciences, 10 Yuanhua Road, Nanjing 210023, China*

⁴*INAF - Osservatorio Astrofisico di Catania, via S. Sofia, 78, 95123 Catania*

⁵*Dipartimento di Fisica “Enrico Fermi”, Università di Pisa, Largo Pontecorvo 3, 56127 Pisa, Italy*

⁶*INFN, Sezione di Pisa, Largo Bruno Pontecorvo 3, 56127 Pisa, Italy*

⁷*INAF-Osservatorio Astrofisico di Arcetri, Largo E. Fermi 5, 50125 Firenze, Italy*

Accepted XXX. Received YYY; in original form ZZZ

ABSTRACT

We introduce the STAR-MELT Python package that we developed to facilitate the analysis of time-resolved emission line spectroscopy of young stellar objects. STAR-MELT automatically extracts, identifies and fits emission lines. We summarise our analysis methods that utilises the time domain of high-resolution stellar spectra to investigate variability in the line profiles and corresponding emitting regions. This allows us to probe the innermost disc and accretion structures of YSOs. Local temperatures and densities can be determined using Boltzmann statistics, the Saha equation, and the Sobolev large velocity gradient approximation. STAR-MELT allows for new results to be obtained from archival data, as well as facilitating timely analysis of new data as it is obtained. We present the results of applying STAR-MELT to three YSOs, using spectra from UVES, XSHOOTER, FEROS, HARPS, and ESPaDOnS. We demonstrate what can be achieved for data with disparate time sampling, for stars with different inclinations and variability types. For EX Lupi, we confirm the presence of a localised and stable stellar-surface hot spot associated with the footprint of the accretion column. For GQ Lupi A, we find that the maximum infall rate from an accretion column is correlated with lines produced in the lowest temperatures. For CVSO109 we investigate the rapid temporal variability of a redshifted emission wing, indicative of rotating and infalling material in the inner disc. Our results show that STAR-MELT is a useful tool for such analysis, as well as other applications for emission lines.

Key words: stars: pre-main-sequence – stars: circumstellar matter – stars: variables: T Tauri, Herbig Ae/Be – stars: individual: EX Lupi, GQ Lupi A, CVSO109 – software: development – software: data analysis

1 INTRODUCTION

Low- and intermediate-mass young stellar objects (YSOs) acquire the majority of their mass in the protostellar phase, but accretion continues during the pre-main-sequence (PMS) phase via an accretion disc over a few million years. Accretion has a large impact on the future of the stars (Hartmann et al. 2016) and the formation of planetary systems (Lynden-Bell & Pringle 1974; Williams & Cieza 2011; Morbidelli & Raymond 2016). The accretion process gov-

erns the transport of matter from the disc to the star and angular momentum from the star to the disc; and therefore affects disc stability, rotation, future stellar activity and potential habitability of planets. This is important for Classical T-Tauri (CTT) stars, with late-type stars observed to remain active during a substantial part of their lives (Gallet et al. 2017). It is also important in Herbig Ae/Be stars, which have masses between CTTs and massive young stellar objects. Such intermediate-mass stars may undergo different accretion mechanisms; from the magnetically channelled accretion of CTTs, to a direct disc-to star accretion through a boundary layer in more massive stars (Mendigutía et al. 2011; Vioque et al. 2018). Disc locking and angular momentum removal by winds/outflows (Shu et al. 1994; Herbst et al. 2002) regulate stellar rotation, but the efficiency of these processes is highly dependent on the accretion

★ https://github.com/justyncw/STAR_MELT

† Based on data obtained with ESO programmes 106.20Z8.002 and 106.20Z8.009.

‡ E-mail: jcampbellwhite001@dundee.ac.uk

rate and the stellar magnetic field (Matt et al. 2012; Cauley et al. 2012).

Accretion and stellar activity also make the detection of young newly-formed planets challenging (Johns-Krull et al. 2016), since these processes mimic and mask both photometric and spectroscopic planet signatures (Crockett et al. 2012; Kóspál et al. 2014). Furthermore, accretion regulates the disc masses and thus affects the migration speeds of both low-mass, non-gap-opening planets (e.g. Tanaka et al. 2002; Paardekooper et al. 2011) as well as massive, gap-opening planets (e.g. Kanagawa et al. 2018). An accretion associated feature such as a magnetospheric cavity may also act as a stopping mechanism of migrating planets (Lin et al. 1996).

It is therefore clear that a thorough understanding of the varying accretion and activity processes for young stars is fundamentally important when studying the evolution of main sequence stars and planetary systems. The main challenge is actually observing the sub-AU scales of accretion and the innermost disc. Whilst the most nearby PMS stars and discs can be studied via interferometry down to a few AU (e.g. Andrews et al. 2016, 2018; Gravity Collaboration et al. 2019), the spatial resolution and sensitivity is still limited, and such accuracy cannot yet be achieved for the overall population of PMS stars that are in general fainter. The innermost part of the disc contains very little gas that is generally warm and thus accounts for low emission contribution, even from facilities such as ALMA (Sicilia-Aguilar et al. 2016). Sub-mm interferometry does also not trace the highly energetic processes related to accretion.

However, the spectra of young stars are known to show many emission lines since the class was defined (Joy 1945). The wealth of metallic emission lines observed allows us to probe the accretion structures, winds, and innermost region of the accretion disc. Investigations of densities, temperatures and spatial locations of material along the line-of-sight using emission lines have been conducted for a small number of PMS stars (e.g. Beristain et al. 1998; Beristain 2000; Sicilia-Aguilar et al. 2012; Petrov et al. 2014b; Antonucci et al. 2017). Furthermore, time-resolved data for many emission lines dramatically improve these results, revealing how far the structures are from the star and their corresponding latitudes (e.g. Sicilia-Aguilar et al. 2015; Schneider et al. 2018; Sicilia-Aguilar et al. 2020a; McGinnis et al. 2020), down to scales not possible with direct imaging techniques. Tracking atomic gas parcels in the innermost disc on short time-scales is also possible - both in emission or absorption (e.g. Mora et al. 2004). Observations conducted over a stellar period (typically ~ 7 days for CTTs, Bouvier et al. 1995) reveal rotational modulations in the emission lines. Furthermore, archival time-resolved data over several years can reveal the long-term variability of accretion structures and activity spots.

High-resolution data of PMS stars are already available from numerous archival programs aiming at spectroscopic planet detection around young stars. These, together with new data expected in the coming years from dedicated surveys, (such as PENELLOPE, Manara et al. 2021, and ODYSSEUS, Espaillat et al. in prep), provide a unique possibility for a comprehensive view of their accretion processes and inner discs. We hence require a means of accurately and precisely analysing such a large quantity of data in a timely manner. In this paper we introduce the STAR-MELT (STellar AccRetion Mapping with Emission Line Tomography) Python package that we have developed to carry out these detailed investigations. The STAR-MELT package is a set of modules and functions to carry out the extraction of the accretion spectrum from the high resolution data, and we foresee many further applications beyond this. We are able to automate the process of identifying, matching and individually fit-

ting emission lines, allowing for quick access to results from a large number of stars, for a diverse range of spectroscopic instruments.

This work is organised as follows: An overview of our emission line analyses is given in section 2. The STAR-MELT package description is given in section 3, followed by example applications of STAR-MELT for three YSOs with different properties, as well as different amounts of data with various sampling cadences, and the corresponding discussion in section 4. Our summaries, conclusions and outlook for the coming years of new data are given in section 5.

2 EMISSION LINE TOMOGRAPHY: INVESTIGATING THE INNER DISC AND ACCRETION STRUCTURES

Observational signatures of accretion in PMS stars are excess emission from x-ray to near infrared (IR). The majority of this emission from the ultra-violet (UV) regime to lower energies predominantly comprises re-processed x-ray shock emission, which originate from the accretion columns and boundary layers (Hartmann et al. 2016). In addition to this excess continuum emission, further key indicators of accretion are the permitted emission lines of e.g. $H\alpha$, $H\beta$, Ca II and He I, which have been used to estimate accretion rates (e.g. Fang et al. 2009; Herczeg et al. 2009; Alcalá et al. 2014). PMS stars also possess many metallic neutral and ionised lines, such as Fe I/II, Ca I/II, Ti I/II, Si II (Hamann & Persson 1992a; Hamann & Persson 1992b; Hamann 1994; Giannini et al. 2013; Alcalá et al. 2014). Because these lines are so persistent, they can be used to map the innermost accretion disc and accretion funnels, and to detect activity-related spots via emission line tomography (Sicilia-Aguilar et al. 2012; Fang et al. 2014; Sicilia-Aguilar et al. 2015, 2017, 2020a).

Although strong lines are most common in strongly-accreting systems (Hamann & Persson 1992a; Hamann & Persson 1992b; Beristain et al. 1998), current instrumentation (such as ESPRESSO, FEROS, HARPS, XSHOOTER, ESPaDOnS) detect He I, Ca II, Fe I/II, Si II, Ti II lines (and more) in the vast majority of young stars (Alcalá et al. 2014), also revealing line velocity changes when comparing spectra taken in different epochs. Extracting the line velocities and profile details, is not immediate. In particular, the velocity modulations observed in narrow lines associated to locations very close to the stellar photosphere (Dodin & Lamzin 2012) will be of the order of the projected rotational velocity ($V \sin i$) based on the system inclination (Petrov et al. 2014a; Kóspál et al. 2014), although other velocity signatures could be due to mass motion of the structures and shocks. Since lines from different species may originate in slightly different places (Dupree et al. 2012), the extraction and analysis needs to address each line individually, fitting the continuum with great care to avoid introducing noise in the result (Sicilia-Aguilar et al. 2015). Moreover, for some lines the underlying photospheric spectrum cannot be neglected and must be subtracted to get the correct shape and velocity of the emission line profile. To obtain further information regarding the physical conditions of the emitting gas (density, temperature), the lines need to be also properly identified and well-fitted.

The emission line tomography technique utilises the time domain to look for distortions in the stellar emission line profiles. It is similar to the application of Doppler tomography, a visualisation technique where the phase and velocity of the line profiles are considered; e.g. applied to the accretion disc of cataclysmic variable stars (Marsh & Horne 1988), or for chromospheric mapping of stellar surface features from UV emission lines (Neff et al. 1989; Busà et al. 1999) and $H\alpha$ plages (Frasca et al. 2008). These previous

studies have applied the technique to more evolved stars, however, the distortions due to accretion have similar spectral signatures. For PMS stars, these temporal distortions can be attributed to rotating spots, winds, accretion funnels, and inner disc structures. Together with approximations of physical properties, including temperatures and densities of the emitting material, we use these Doppler signatures of metallic emission lines to obtain tomographic information regarding the accretion structures, activity (hot) spots and the innermost hot atomic gas in the disc. The metallic lines observed in high resolution spectra of young stars span a large range of excitation potentials and transition probabilities. This allows us to probe various depths, densities and temperatures over a few stellar radii along the accretion columns, shocks, and post-shock regions, and to detect winds and hot spots.

2.1 Physical approximations from line ratios

In addition to investigating the line profiles and temporal variations to make tomographic inferences about the inner-disc and accretion in PMS stars, physical approximations can be drawn from the data by comparing the observed line ratios to those of theoretical calculations. At present, STAR-MELT includes two simple methods that allow to compare the relative line intensities for ionised and neutral species using the Saha equations (Mihalas 1978; Hubeny & Mihalas 2014), as well as to constrain the temperature and column density-velocity gradient for broad lines using the Sobolev approximation for lines originating in the same upper level (Beristain et al. 1998). Both methods have been applied in the past to different observations of young stars (e.g. DR Tau, EX Lupi and Z CMa; Beristain et al. 1998; Sicilia-Aguilar et al. 2012, 2020a). Whilst these routines are automated within STAR-MELT, caution needs to be exercised for individual objects; such as ensuring lines are selected as likely originating from similar locations (i.e. similar line profiles), or from similar wavelength regions to avoid extinction influences. Furthermore, deviations from Local Thermodynamic Equilibrium (LTE) including non-thermal ionisation, pumping of the upper levels of some lines by higher-energy transitions, radiative transfer effects including optical depth and self-absorption, and saturation are among some of the processes that can be encountered in YSOs and that may limit the use of these approximations for certain targets and/or lines.

The Saha equation 1 (Mihalas 1978) allows to determine the relative populations of ionised and neutral species,

$$\frac{n_{j+1}n_e}{n_j} = \left(\frac{2\pi m_e kT}{h^2} \right)^{3/2} \frac{2U_{j+1}(T)}{U_j(T)} e^{-\chi_1/kT}, \quad (1)$$

where n_{j+1} and n_j are the densities of the two species, n_e is the electron density, T is the temperature, m_e is the electron mass, k and h are Boltzmann and Planck's constants, respectively, χ_1 is the ionisation potential, and $U_x(T)$ is the partition function for species x . The equation assumes that the species are in LTE, so that the population between different levels can be estimated using the Boltzmann statistics,

$$\frac{n_i}{n_0} = \frac{g_i}{g_0} e^{-E_i/kT}. \quad (2)$$

Here, the population of an excited level i is given with respect to the ground level, as a function of the temperature, the energy of the upper level E_i , and g_x is the statistical weight of level x . The relative intensities of the lines will depend exclusively of their atomic parameters.

Because in general the spectra are not flux-calibrated, the Saha

calculation is performed in STAR-MELT as done in Sicilia-Aguilar et al. (2020a), using the relative intensities observed between selected lines to compare to the relative intensities derived from Saha models spanning a range of temperatures and electron densities, and estimating as best fit the one that results in a lower standard deviation between the values associated to all the lines. The uncertainty is derived including the regions where the standard deviation value is up to 3 times the minimum value, and the contribution of individual lines is weighted according to the quality of the atomic parameters as listed in the National Institute of Standards and Technology (NIST) database¹.

The Sobolev approximation, when applied to lines arising from the same upper level, allows us to overcome the radiative transfer effects that can change the relative populations of the various atomic levels (Beristain et al. 1998). Its main limitation is that it should only be applied to broad lines, since it uses the Large Velocity Gradient (LVG) approximation to treat the escape probabilities. Considering two lines from the same upper level, the ratio of the weakest to the strongest line ($r_{w/s}$) can be written as

$$r_{w/s} = \frac{A_{ki}^w \lambda_s}{A_{kj}^s \lambda_w} \frac{1 - e^{-\tau_w}}{\tau_w} \frac{\tau_s}{1 - e^{-\tau_s}}, \quad (3)$$

where A_{ki}^x is the transition probability, λ_x is the wavelength, and τ_x is the opacity for line x . The LVG approximation allows to rewrite the opacities as

$$\tau = \frac{hc}{4\pi} \frac{n_i B_{ik} - n_j B_{ki}}{dv/dl} \approx \frac{hc}{4\pi} B_{ik} g_i \frac{e^{-E_i/kT}}{U(T)} \frac{ndl}{dv} \quad (4)$$

where the previously used symbols retain their meanings, and c is the speed of light, B_{xy} are the Einstein's coefficients, and we have introduced $N = ndl/dv$, the modified column density or density-velocity gradient.

This approximation allows us to estimate the best-fitting density-velocity gradient and temperature for every pair of lines from the same upper level. The calculation resulting from a single pair of lines will be degenerated regarding both variables, but we can use all pairs of lines to derive further constraints. The main theoretical limitations of this method are those imposed by LTE and the LVG approximation, but one needs to consider further experimental constraints, in particular, in case of lines with large uncertainties in their atomic parameters and with similar strengths.

In general, none of these methods should be used to compare lines that have different profile types and/or velocities, since this is indication that the lines have different origins. Comparing lines in very different parts of the spectra can also affect the results if calibration varies across the wavelength, or due to extinction. In future work we will see if including an extinction law to different wavelengths will allow this method to function across larger ranges.

3 THE STAR-MELT PYTHON PACKAGE

We have designed the STAR-MELT Python package to automatically carry out as many as possible of the steps required to map the accretion and inner disc of PMS stars, whilst facilitating user interaction as needed. Broadly, this covers reading in the data for a given target star and spectroscope, determining the radial and rotational velocities using a template/standard star, identifying and

¹ https://physics.nist.gov/PhysRefData/ASD/lines_form.html

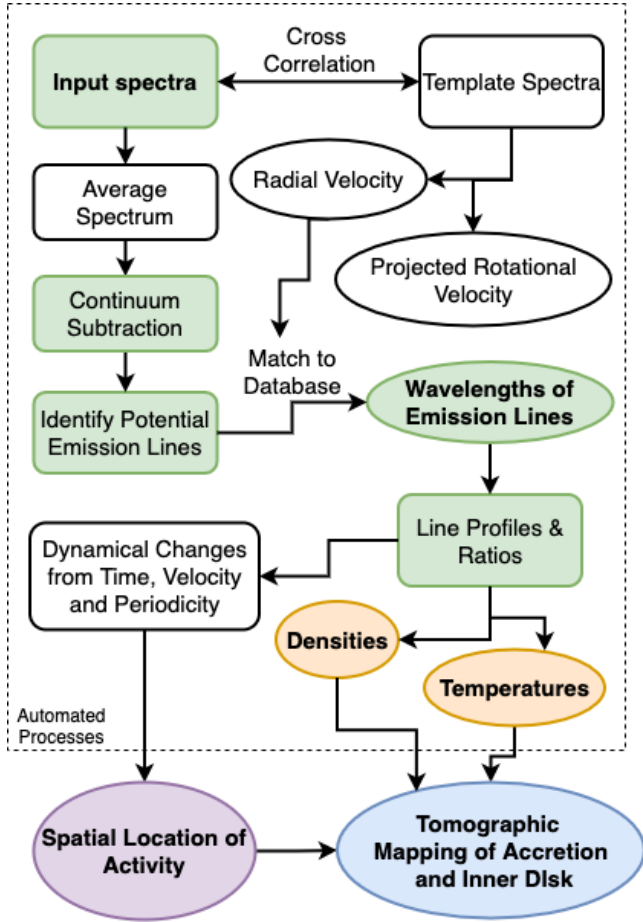


Figure 1. STAR-MELT flow chart, outlining the key steps in the package workflow. Steps within the outer dashed box are carried out automatically, subject to selection of emission lines for profiles and subsequent steps.

matching the atomic emission lines to a reference database, and various visualisation and analysis functions (Fig. 1). There are also several convenience functions to handle reading in data, customising output plots and exporting results. Further interactivity with STAR-MELT is achieved via the use of Jupyter Notebooks. This allows for dropdown widgets and sliders, such that one could run the STAR-MELT Jupyter notebook on their own data without the need of editing any code². The STAR-MELT package features multiple modules and functions to also allow for a fully scripted automation for obtaining summary statistics of the specified data, such as number of emission lines identified/fit (optionally for specific elements) for all target stars across all observations. STAR-MELT uses various *ASTROPY* (Astropy Collaboration et al. 2013, 2018) functions, in addition to further package dependencies that will be referenced in their corresponding descriptions in this section.

The relevant data are extracted directly from the reduced FITS spectra³. The STAR-MELT analysis functions are designed to be compatible with a simple wavelength, flux and (optional) error data frame, for a given (modified-) Julian date observation. These can be

user provided as a csv or text file from any instrument source; with a simple routine that will create the required data frame. However, there is further information that is extracted from the FITS headers that will aid in the analysis flow and it is recommended to use the integrated STAR-MELT read-in functions. The mean and median flux values for each set of observations are determined and also stored in the data frame of observations. There is a further option here to normalise/scale the flux data frame, by dividing each flux value by the median flux across the observation. This is useful for comparing data from different instruments.

Some spectroscopes have gaps in the wavelength coverage, which are automatically removed for each instrument where applicable. As are regions of the wavelength range badly affected by telluric absorptions, such as 6872 - 6920 Å and 7592 - 7690 Å (Curcio et al. 1964). Further wavelength exclusions can be specified by the user for all observations. Similarly, one can also choose to consider a smaller wavelength range than that automatically obtained from the FITS data. The user can also specify at this stage which of the observations (dates) they wish to analyse. This is particularly useful for large amounts of archival data, covering many years.

3.1 Radial and Rotational Velocities

Radial and projected rotational velocities (RV and $V \sin i$, respectively) of the target star are calculated using the standard cross correlation function (CCF) with a template star of similar spectral type⁴. Table A1 shows the list of standard stars provided in the STAR-MELT package library at the time of publication.

To automate this process for any target star, a SIMBAD query is performed⁵ on the name (identifier) of the target star to pull the most recent spectral type. STAR-MELT then selects the standard star with the closest spectral type from the STAR-MELT library. Since the RV of the target PMS stars may be variable, unavailable, or not well defined, we do not pull that information from the SIMBAD database; instead, the user can calculate it within STAR-MELT or supply it manually. The RV of the standard star, which is well defined, is queried from SIMBAD to allow for the calculations. Obtaining the RVs for the standard stars from SIMBAD allows for further standard stars to be added in future releases, or for the user to provide their own standard stars. STAR-MELT can also compute the CCFs using modelled stellar atmosphere spectra as the template. This is useful for checking that the value obtained from the standard star is correct, and for where the standard star spectral type does not well sample the target star.

Whilst the user can specify a specific observation for which to calculate the RV and $V \sin i$, for the purposes of emission line identification, we use the median spectra across all observation dates considered. This avoids the introduction of uncertainties for each observation, leaving instead only a potential systematic offset. Providing the wavelength calibration of the reduced data is accurate, errors of a few km/s in the RV calculation would not have a large impact on matching the emission lines to the reference database. To improve the velocity accuracy for FEROS, we do, however, apply a manual barycentric correction to velocities calculated from the FEROS pipeline (Müller et al. 2013). Note that for cases where we intend to study the relative radial velocity variations for the lines,

² A tutorial Jupyter Notebook for STAR-MELT is provided within the [GitHub repository](https://github.com/sczesla/PyAstronomy).

³ See the online documentation for the up-to-date list of direct FITS instrument compatibility.

⁴ Using the *PYASTRONOMY* <https://github.com/sczesla/PyAstronomy> functions `CROSSCORRV`, `ROT Broad` and `FASTROT Broad` (Czesla et al. 2019).

⁵ Using *ASTROQUERY* (Ginsburg et al. 2019)

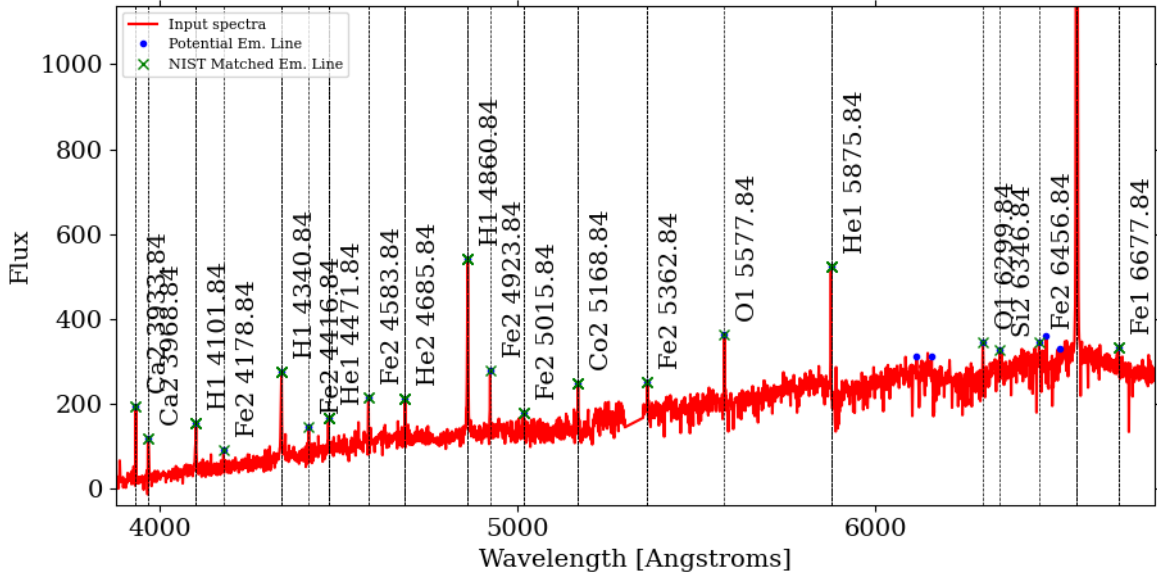


Figure 2. Emission lines identified from the median spectra of EX Lupi HARPS observations. The S/N threshold at which to identify potential lines defaults to 3σ and can be specified by the user. Potential lines are indicated by the blue circles, with the green crosses showing those that have been successfully matched to the NIST database, within the velocity and wavelength tolerance. For the line labelling, if a line has a multiple match to the database, only the closest match will be displayed in the plot (all matches are given in the resulting list and will be filtered/selected in the following steps).

we recommend to derive the stellar radial velocity for one spectrum (e.g. the average or highest S/N spectrum) and use it for the rest. Therefore, the uncertainties in the line radial velocity would depend only on the line fit and on the accuracy of the wavelength solution provided by the telescope.

Our analysis primarily uses the $V \sin i$ for specifying the velocity range in which to match the emission lines (as discussed in Sec. 2). Hence, for fast rotators where the $V \sin i$ calculation fails due to rapidly increasing CCFs, we assume a value of 50 km/s and set the corresponding range for velocity windows.

At present, STAR-MELT does not include any veiling correction nor estimate of the spectral type. In particular, veiling is not addressed because we intend to use STAR-MELT to study the prevalence of line-dependent veiling (Dodin & Lamzin 2012), which is known to affect spectral types, radial, and rotational velocity estimates and can have particularly dramatic effects in radial velocity estimates for stars with many lines (Kóspál et al. 2014; Sicilia-Aguilar et al. 2015), but this needs to be kept in mind when comparing with other results and line ratios from different spectral ranges. However, STAR-MELT is compatible with output from the ROTFIT reduction software (Frasca et al. 2003, 2006; Molenda-Żakowicz et al. 2013), which we use in this work to check that our results are not affected by photospheric absorption in the lines.

3.2 Automatic Emission Line Identification

With the RV of the target star determined, we are now able to automatically identify and match the emission lines to our reference database (Fig. 2). The database provided with the STAR-MELT package is compiled from the NIST database⁶ (Kelleher et al. 1999;

Ralchenko et al. 2005; Kramida, A. et al. 2020). All neutral and singly ionised atomic transitions (for lines with transition probabilities) from elements H through Zn are included for the air wavelength range of 3000–20000 Å. This includes information about the wavelength, excitation potential (or energy of the upper level, E_k in eV), multiplicity, relative intensity, and transition probabilities (or Einstein coefficient for spontaneous emission, A_{ki}), each of which are required in our analysis. Constraints on the transition probabilities and energies of lines can be applied before or after the matching process. By default, the wavelengths in air are used for the matching. The vacuum wavelengths are also included in the database and can be optionally used in the matching process⁷. During the matching process, we also indicate previously observed lines from the spectra of EX Lupi, ASASSN-13db and ZCMa (Sicilia-Aguilar et al. 2012, 2015, 2017, 2020a), which can help the user to identify common lines in case of doubt.

Emission lines are automatically extracted by roughly subtracting the continuum contribution from the median-scaled flux values, using sigma-clipping, and then applying a SciPy Savitzky-Golay (S-G) filter (Savitzky & Golay 1964).⁸ The filter is a standard interpolative polynomial smoothing filter, we used a coefficient length of 31 with a default 3rd order polynomial; both of which can be modified by the user. These default values were a good balance between smoothing out the narrow lines completely, and only applying a

⁷ A further vacuum wavelength range of 2–50 Å is also included for X-ray data, which is not discussed in this paper but will be expanded upon in future work.

⁸ STAR-MELT can, in principle, also detect absorption lines in the same manner, by using the lower threshold instead of the upper. Since this was not a main intent when designing the package and carrying out our analysis, the absorption line detection requires further testing.

⁶ <http://physics.nist.gov/PhysRefData/ASD/linesform.html>

minimal local shift around broad lines (see Sec. 4 for further details on the adjustments made for different types of line identification). This continuum subtraction process works well for stars with spectral types B through M. The peaks of the emission lines are then identified via another stage of sigma-clipping at a user-specified threshold level.

The wavelength positions of these identified lines are then shifted by the stellar RV contribution and matched to the reference line list, with a default absolute tolerance of 0.2 \AA . A further constraint is then applied to check that the shift introduced by the RV is less than the dispersion resulting from the $V \sin i$. This absolute and velocity tolerance can also be set by the user for broader or highly shifted lines.

The positional list of matched lines are saved as a data frame, along with the corresponding atomic properties from NIST. This can be downloaded and stored locally. It can also be re-read by the package so that future analysis can refer back to the already determined list of lines. If an identified line has more than one possible match in the database, this is indicated by the ‘multi’ column in the data frame; allowing the user to further investigate which of the lines are the most likely matches (see notes to Fig. 2). The steps thus far in the STAR-MELT package are computationally inexpensive, with the largest increase depending on the number of observations. It is possible that some lines are misidentified due to noise in the spectra. Further refinement to the matched lines can be completed by fitting simple models to the line profiles.

The model line fitting used in STAR-MELT employs a goodness of fit measure to remove badly fitted (and potentially misidentified) lines, hence producing a final list of refined matched lines. Again, all such information can be downloaded at any stage for future reference. The line fitting has to be carried out on a one-by-one basis, taking some time to fit all identified lines (tests result in ~ 20 minutes for ~ 500 lines, using a computer with a 2.3 GHz Quad-Core Intel Core i5 processor and 16 GB 2133 MHz LPDDR3 RAM). Therefore, if the user does not wish to carry this out for all of the lines, selections can be made from the list of matched lines to decide which ones to fit, for example, all Fe lines with an excitation energy less than a given value. With the selections made for which lines to fit, the user then specifies for which observation dates, or average spectra, they would like to fit the lines for. If an overview of the lines is required, the average spectra yield much better signal/noise ratio than the individual lines. If temporal investigations is preferred, all observation dates of interest can be selected and fit.

3.3 Line Fitting

To perform the line fitting, STAR-MELT uses the Python package LMFIT⁹ (Newville et al. 2014), which carries out non-linear least-squares model fitting. The advantage of using the LMFIT package is that parameter attributes (such as the central position, or σ values) for the variables used in the model fitting can be either be automatically obtained and set from the observational data itself; or manually constrained by the user. In the case of the latter, the constraints can be set interactively within the Jupyter notebook, and do not require the editing of any code. Furthermore, all best-fit model parameters, along with the model data, are easily obtained from the model class. Since the line profiles may be very complicated, STAR-MELT is designed to provide simple, yet accurate, model fits that allow for detailed comparisons of parameters.

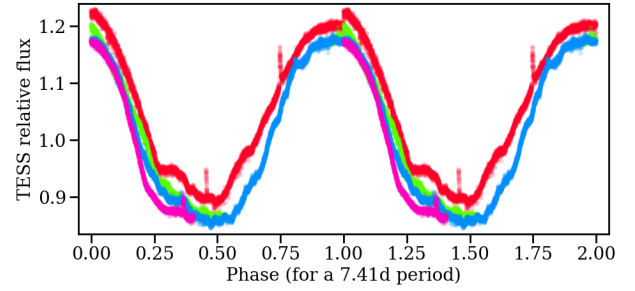


Figure 3. *TESS* data for EX Lupi, wrapped according to the 7.41d period. The data are colour-coded according to different period cycles.

Up to four Gaussian components can be fitted for each emission line. The default fitting option is to adopt a model comprising one Gaussian plus a linear component to approximate the emission line plus the continuum, respectively. For lines that possess better signal/noise (S/N) and/or more complexity, up to two more positive Gaussian components can be included. A second positive Gaussian can identify narrow components within broad components of the lines (e.g. figures within CVSO109 discussion, Sec. 4.3). A negative Gaussian can also be combined with any of these positive Gaussians, which can model absorption components from winds/outflows/infall (e.g. figures within GQ Lupi A discussion, Sec. 4.2). In addition to the component parameters, the module also returns calculated parameters such as the integrated flux and line asymmetry. The option to fit further line profiles, such as Lorentzian and Voigt models, will be incorporated in future development of the package. A minimum goodness-of-fit (the reduced χ^2 statistic) can be specified to only return those fits meeting the criteria, and thus provide the user with a set of well-fitted, identified emission lines. This helps to remove spurious lines or those that are not present on certain dates.

With the selections made for which lines to be fitted specified (such as a given set of elements with a maximum excitation potential), the fitting process described above is then fully automated within STAR-MELT. The list of matched emission lines is used to subset the main flux data frame around the given wavelength range for each identified line. This function is also a convenience function that can be called to produce a plot of the lines, with either wavelength or velocity as the dependent variable. For the line fitting, the velocity dispersion around the specified line position is required. The velocity range to consider can be specified from the $V \sin i$ of the star, or be manually set by the user. When fitting multiple lines, this is carried out iteratively for each identified line from the previous STAR-MELT functions.

Whilst line profiles can be explored directly from the reduced observational data, which require more individual, bespoke analysis and discussion, the parameters from the model-fits such as the central positions can be used to generate periodograms to probe overall variations for the temporal variability of the emission lines. The integrated flux values from the model-fits can be used to calculate observed line ratios, which can be compared to their theoretical counterparts, as described in Sec. 2. Further discussion and examples are given in our analysis of three YSOs in Sec. 4.

In terms of the STAR-MELT work-flow, we have now obtained the necessary analytical information from the observational data to fully investigate the emission lines across our observations. Although there are various options the user may wish to specify for their data, all such options have default values. Thus, in principle,

⁹ <https://lmfit.github.io/lmfit-py/index.html>

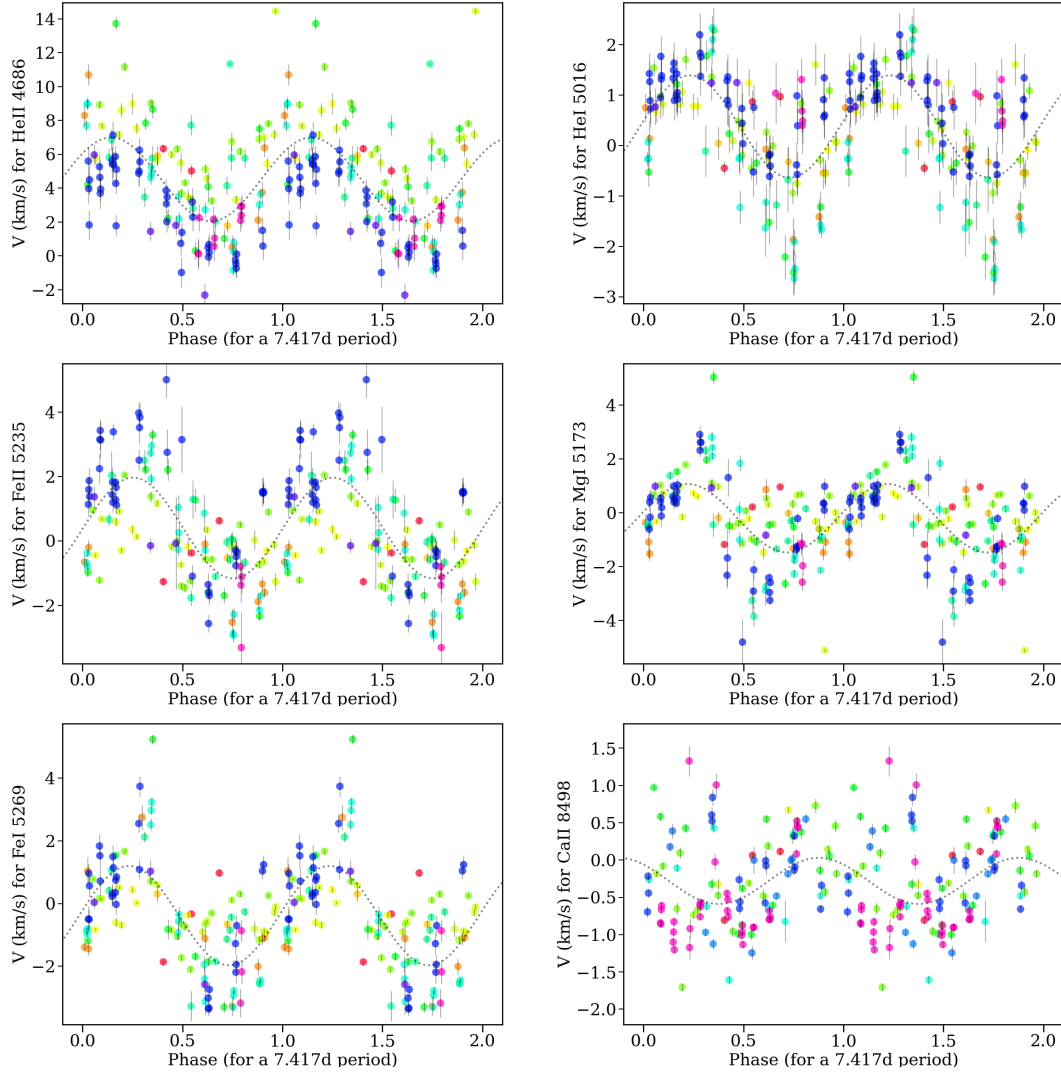


Figure 4. Some examples of periodicity observed in the velocities of the lines extracted with STAR-MELT for EX Lupi, all of them wrapped with the 7.417d period obtained for the He II 4686 Å line. The colour scale is set to reflect the number of periods elapsed since the first observation, and changes from red to purple from the first to the last MJD displayed. The dotted line is the best fit for the expected modulation (equation 5). The phase for the He II 4686 Å and Ca II 8498 Å lines are notably different from the rest.

everything up to this stage can be fully automated by STAR-MELT, with good compatibility with the different instruments. The physical approximations described Sec. 2, and the following discussion section pertain to stellar accretion investigations. However, it is clear that up to here, STAR-MELT has numerous potential applications to aid in identification and fitting of all kinds of astronomical emission lines. The STAR-MELT package is available to the community on [GitHub](https://github.com/justyncw/STAR-MELT)¹⁰, along with an example Jupyter notebook that features all steps outlined in this Section and example data from this work. The STAR-MELT notebook can be run in an online executable environment via the [binder platform](https://mybinder.org/v2/gh/justyncw/STAR-MELT/HEAD)¹¹. We also welcome collaborative projects using the package.

4 STAR-MELT APPLICATION & DISCUSSION

The application of STAR-MELT is demonstrated by analysing three YSOs: EX Lupi, GQ Lupi A and CVSO109. We have studied EX Lupi in previous work (Sicilia-Aguilar et al. 2012; Kóspál et al. 2014; Sicilia-Aguilar et al. 2015), and we detail here the comparisons of the results achieved using STAR-MELT; along with investigations of the YY Ori-type profiles in GQ Lupi A and variability analysis of CVSO109 from the ongoing PENELLOPE survey (Manara et al. 2021).

4.1 EX Lupi

EX Lupi is a M0 star (Herbig 1977; Sipos et al. 2009; Alcalá et al. 2017) and the prototype of EXor variables; a class of low-mass young stars with repetitive accretion-powered outbursts that recur within timescales of months to years (Herbig et al. 2001; Herbig 2008). Although very large outburst where the accretion rate increases by 2-3 orders of magnitude or more are rare and have

¹⁰ <https://github.com/justyncw/STAR-MELT>

¹¹ <https://mybinder.org/v2/gh/justyncw/STAR-MELT/HEAD>

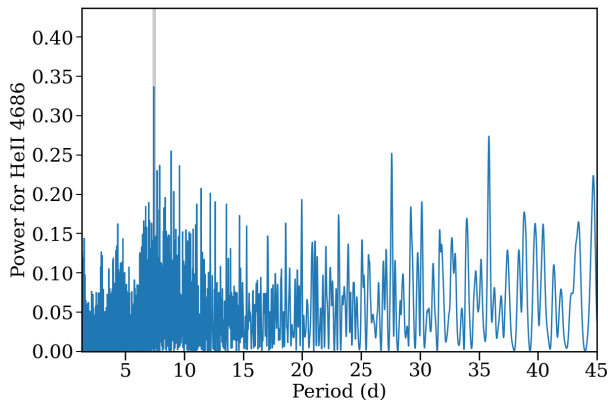


Figure 5. Lomb-Scargle periodogram revealing the 7.417d period from the radial velocity of the He II 4686 Å line as observed for EX Lupi.

been documented only twice in the 1950's and in 2008 (Herbig 1977; Jones 2008), smaller accretion variations are observed on a regular basis (Lehmann et al. 1995; Herbig 2007; Sicilia-Aguilar et al. 2015) and we are considering them as part of the quiescence stage.

EX Lupi spectra contain a wealth of emission lines in both outburst and quiescence, with complex profiles that include broad and narrow, strongly variable components (Aspin et al. 2010; Sicilia-Aguilar et al. 2012, 2015). The broad components are more evident in outburst and at times when the accretion rate is high. The narrow lines are present at about all times (with some variations in intensity and S/N) and originate in the accretion post-shock region at the footprint of the accretion column over the stellar surface. The lines display rotational modulation in quiescence, which is a signature of the accretion structures being remarkably stable over time (Sicilia-Aguilar et al. 2015).

Because of the number of lines and their stability, EX Lupi is an ideal target to test the capabilities and functionality of STAR-MELT. We used the data available for EX Lupi during its quiescence period, which contains the epochs that have been studied in more detail regarding line velocities and periodicities (Sicilia-Aguilar et al. 2015), plus some more recent data. These include the data obtained with FEROS, HARPS and ESPaDOnS (see Appendix B for instrument descriptions). We use the data from 2007-2012 that had been previously analysed (excluding the data from the 2008 outburst; Kóspál et al. 2014; Sicilia-Aguilar et al. 2015), together with archival observations obtained between 2013-2019, with a total of 152 observations (see Tab. C1). Although we exclude the data obtained during the large 2008 outburst, the data cover epochs where the accretion varies between a factor of few to one order of magnitude. For the analysis, regions strongly contaminated by telluric features were excluded, which affects the 5500-5700, 6760-6970, 8150-8390, and 9100-9250 Å ranges, primarily. The radial velocity of EX Lupi (around 0 km/s) is recovered (-0.05 ± 0.33 km/s) by STAR-MELT. The $V \sin i$ derived has an upper limit of 5 km/s, with the main limitation being the slow rotation of the target compared to the STAR-MELT template. This value is consistent with the previously determined $V \sin i$ of $\sim 4.4 \pm 2$ km/s (Sipos et al. 2009), which we adopt in the following analysis.

Careful continuum sampling was found to be important for the extraction of the broadest lines (such as the H Balmer series or the Ca II IR triplet). In general, averaging over a window of 2 Å and fitting the continuum with a 3-degree polynomial produced the best result overall to extract the metallic lines. The continuum becomes

uncertain in the proximity of very broad lines, so that for stars with very different types of line profiles, it is more efficient to run STAR-MELT twice and extract and fit separately the broad and the narrow lines. Our analysis here is based on the narrow metallic and He lines, which have FWHM under 50 km/s.

Because the lines are in general broad, we experimented with various criteria for automated line finding. The best criterion to identify a maximum number of lines while minimising the contamination by features that are not real was found to be between 2 and 2.5σ , where σ corresponds to the standard deviation per pixel of the continuum. The main issues observed in the automated line identification occurred in the regions with telluric features, as well as for lines that appear both as a narrow emission and a photospheric absorption feature. Those include a large number of the Fe I lines (see Sicilia-Aguilar et al. 2015), and a detailed photospheric fit with a template with a similar spectral type will be needed to be able to extract such lines, to be implemented in the future. Non-existing lines identified automatically in regions where the continuum is uncertain due to tellurics, bad pixels, or nearby strong lines can be easily filtered out by fitting the lines. The best fitting window depends on the line properties, and thus for instance the broader He I and He II lines were best fitted using a window of ± 50 km/s, while narrower Fe I and Fe II lines can best fitted with a ± 25 km/s window.

All the strong lines flagged in Sicilia-Aguilar et al. (2015) could be recovered and fitted (see Tab. D1). One of the main potential issues of the automated continuum fit could be to introduce noise in the velocity of the lines that invalidates the periodicity studies (Kóspál et al. 2014). Reproducing the periodic velocity signatures observed in Sicilia-Aguilar et al. (2015), who reported a rotational period of 7.41 d, is thus a good test for the robustness of STAR-MELT. This period is now also confirmed by TESS data (see Fig. 3) obtained via the Barbara A. Mikulski Archive for Space Telescopes (MAST¹²). The periodicity observed in the lines is clearly recovered (see Figs. 4 and 5), as well as the offset in the phase between the very energetic He II line and the Fe lines. As previously found, the modulation is weaker in very strong lines that are expected to be produced over larger and more distributed regions around the stellar surface, but has improved in significance when extracted with STAR-MELT. For instance, the modulation for the Ca II IR lines, despite having a very small amplitude, produces cleaner results when extracted more consistently with STAR-MELT; and suggests a difference in phase with respect to the rest. This could indicate varying temperatures on the hot spot(s) over the stellar surface, and will be studied in detail subsequent work. Shorter periods and worse-defined rotational modulation can be also a signature of more than one spot (or a more extended region in longitude) producing line emission. In general, we find that the STAR-MELT extraction is more self-consistent and the possibility of choosing a fitting window appropriate for each line improves the results even for the weaker lines that have lower peak-to-peak amplitude in their velocity modulations.

As in Sicilia-Aguilar et al. (2015), the amplitudes of the observed modulations can be related to the latitude of the spots that originates them. We observe the same trend, with the He II line displaying the largest amplitude, Fe II lines having amplitudes around 1-2 km/s, and Ca II IR lines having often a nearly-negligible modulation. STAR-MELT can more efficiently extract some of the lower energy lines such as Fe I and Mg I, revealing now significant modulations. This, together with the increased number of datapoints,

¹² <https://mast.stsci.edu>

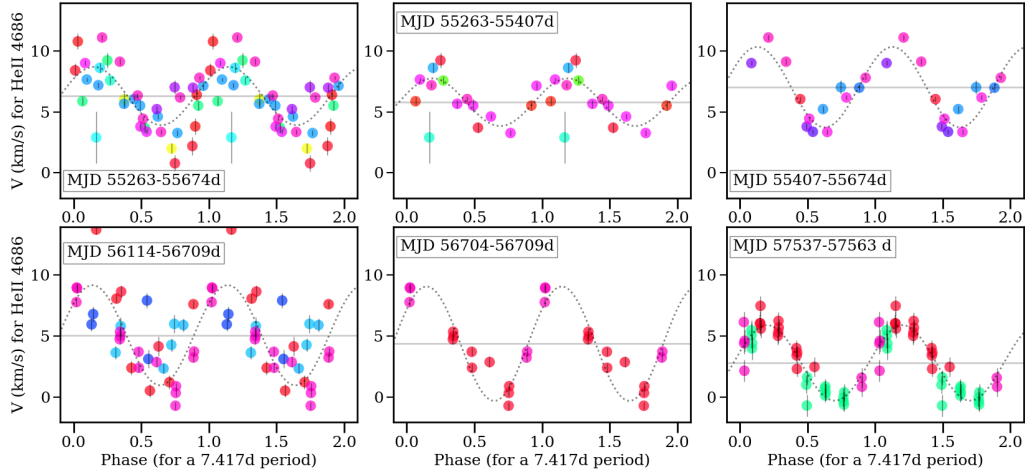


Figure 6. Example of longer timescale variations observed in the He II line for EX Lupi, for different timescales and epochs. Only data with goodness-of-fit < 0.1 are plotted. The colours indicate the epoch at which the data were obtained, as a continuous scale from red (the initial MJD) to purple (the final MJD). The dotted line is the best fit for the expected modulation (equation 5). The horizontal line shows the offset or central position of the modulation (V'_0).

allows us to estimate the rotational period from many other lines, confirming that the large majority of lines are consistent with a rotational modulation with period ~ 7.4 d (see Table E1), with the exceptions found for lines with few points and/or low amplitude. In general, the modulation can be written as

$$RV_{line} = V'_0 + v \sin i \cos \theta_s \sin \phi, \quad (5)$$

where V'_0 is an offset velocity after correcting for the stellar radial velocity (which may depend on any residual motion such as infall, on optical depth effects, and may also have a non-negligible systematic uncertainty for some lines¹³), $V \sin i$ is the projected rotational velocity, θ_s is the latitude of the spot, and ϕ is the phase. Results for some lines are given in Tab. E1. Therefore, for lines originating on a spot at or very near the stellar surface, the maximum modulation observed will be $V \sin i$ (Bouvier et al. 2007). This is consistent with our observations, confirming the origin in the post-shock region at the footprint of the accretion column and very close to the stellar surface. Lines originating in a raised structure could have modulations larger than $V \sin i$.

The amplitude and phase of the line radial velocity modulation thus depends on the location of the spot. In addition, a double or multiple surface spot would tend to produce a shorter period (e.g. as observed in RX J1604.3-2130A; Sicilia-Aguilar et al. 2020b), and in general, emission originating from more than one structure (e.g. over the surface and/or along an extended accretion column) could dilute the rotational modulation. For lines with rotational modulation and radial velocity amplitudes below $V \sin i$ we can therefore assume that the spot is very close to the stellar surface and thus derive its latitude and relative phase. The results of this exercise are listed in Table E1 and shown in Figure 7. STAR-MELT allows us to extract lines with higher accuracy. The amplitudes of the modulations for all lines are higher as extracted with STAR-MELT compared to previous, more manual extraction (Sicilia-Aguilar et al. 2015), and the uncertainties in the phase are lower. The improved

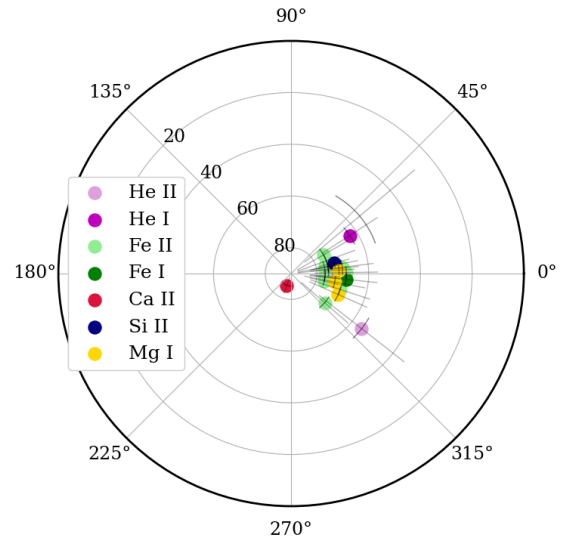


Figure 7. Location of the line-emitting region for different species for EX Lupi, assuming that it is located on the stellar surface. The lines are labeled according to their species, and the data is shown in polar coordinates, with the stellar pole closer to our line-of-sight in the centre. The relative phase of the lines is converted to longitude over the stellar surface.

line fits constrain the location of metallic lines to a small spot on the stellar surface, which is visible at all times. The main uncertainty in the latitude does not come from the method, but reflects the fact that the line amplitudes vary in time, which is an indication of a possible change in latitude over the stellar surface, and/or vertically. The uncertainty in $V \sin i$ would produce a systematic offset.

The differences in phase and amplitude between the He II line and the rest (Sicilia-Aguilar et al. 2015) are also confirmed, although the new data also reveal that the amplitude of the He II line is very variable over this longer period of time (see Figure 4). Such a phase difference may indicate a temperature structure either along the stellar surface or on the vertical line, with line emission from material at slightly different latitudes or heights over a vertically-

¹³ Different references provided by NIST often give line wavelengths with systematic differences of 1-2 km/s, so that line-to-line zero-point variations below this level have to be treated with extreme caution. Note that such an offset is systematic, so relative radial velocity variations are not affected.

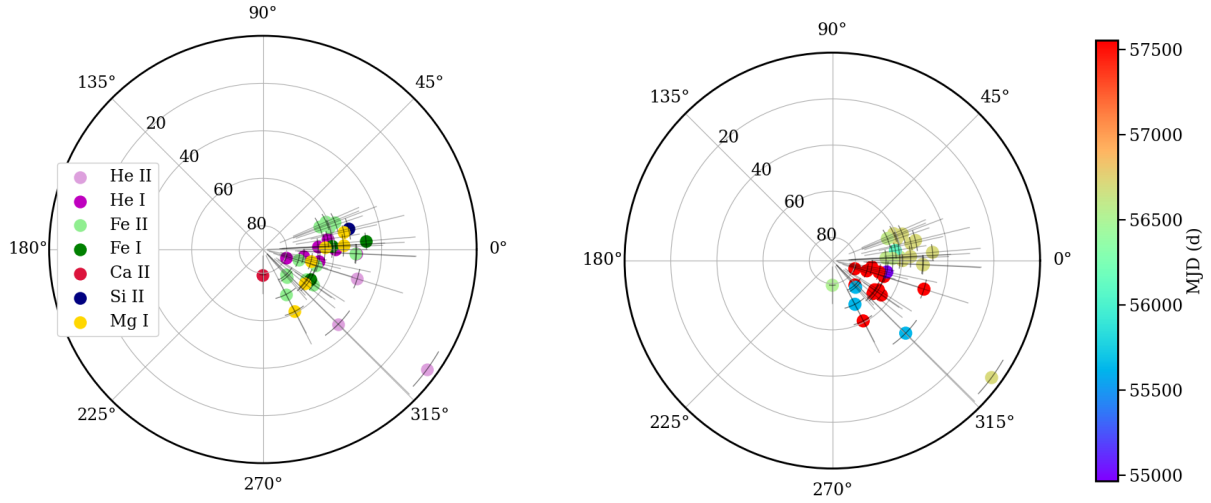


Figure 8. Location of the line emission in EX Lupi, assuming that the spot is located on the stellar surface. The location is derived by fitting the line radial velocity for various time intervals that contain a significant number of points. The left panel displays the location of lines from various species. The right panel shows the variation according to the central MJD of the corresponding interval.

extended column. The lines are also weaker during periods of lower accretion, which causes some of the lines to not be detected across all epochs, although the periodicity remains the same.

There is evidence for longer-term variations in offset velocity, amplitude, and phase (see Fig. 6). To disentangle the effects of time variations from variations in spot properties over the stellar surface, we fitted Eq. 5 to the radial velocity of the strongest lines in different MJD intervals (see Figure 8 and Table E2). The time intervals were set by the requirement of having at least 10 datapoints for the fit to be significant. This means that they include several periods and have a duration of weeks to nearly a year, which may dilute any variations occurring on shorter timescales. The conclusion is that, although there are clear latitude and longitude variations in the location of the line-emitting region, this location remains small (spot-like) and within the same quadrant during the nearly 7 years for which the time analysis is possible. Therefore, the filling factors of the line-emitting region remains always small, which could also explain the very high temperatures observed despite the low quiescence accretion rate.

The second result we tested with STAR-MELT is the temperature ranges observed in EX Lupi. Two main sets of lines can be used for this, including the He I/He II and the Fe I/Fe II lines. The results for He are consistent with the high temperatures (over 20,000 K) estimated in Sicilia-Aguilar et al. (2015) (see Fig. 9). The very high temperatures and densities (e.g. compared to Hartmann et al. 2016) indicate, as had been pointed out before, contributions of non-thermal ionisation. This is one of the main limitations of the calculation, together with the fact that the line profiles differ slightly between ions and neutrals, so that as before, the results are dominated by the single He II line and probably suggest a temperature higher than the regions where much of the more extended wings of He I are produced. There are a total of 20 Fe I/II lines that are identified and strong enough to produce reliable fits. Among those, two of them show very large velocity offsets (>3 km/s in absolute value) that suggests that they may correspond to different species and were thus excluded from the analysis. The remaining 18 produce a significantly lower temperature compared to He, as expected. Further selection based on data quality and on similar wavelengths (4900-5400 Å) to minimise possible effects of variations of the un-

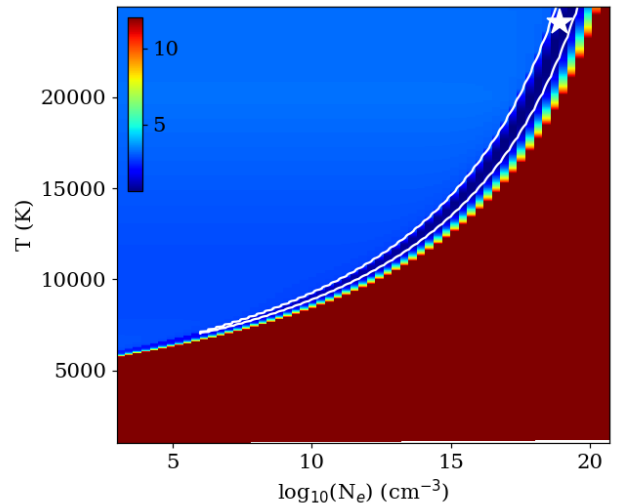


Figure 9. Results of the Saha equation applied to the 7 He lines identified in EX Lupi by STAR-MELT. The colour scheme represents the relative variations in the line intensity ratio for each combination of temperature and electron density (such that 0.1 would correspond to 10% average deviations). The white contour marks the regions for which the relative variations of the line ratio are up to 3 times the minimum value observed, which is considered as our best-fit region, and a white star mark the best fit.

derlying continuum tighten further the result (see Fig. 10, left and middle). One of the main limitations of the Fe I/Fe II result is that at present, many of the weaker Fe I lines are not well-fitted due to the presence of photospheric absorption, which will be addressed in future versions of STAR-MELT.

We also show the results from the Sobolev LVG approximation for a pair of Fe II lines that originate from the same upper energy level (Fig. 10, right). These lines are relatively broad, hence we can assume that the LVG approximation holds true. Both lines were fitted across each individual spectra, using the default goodness-

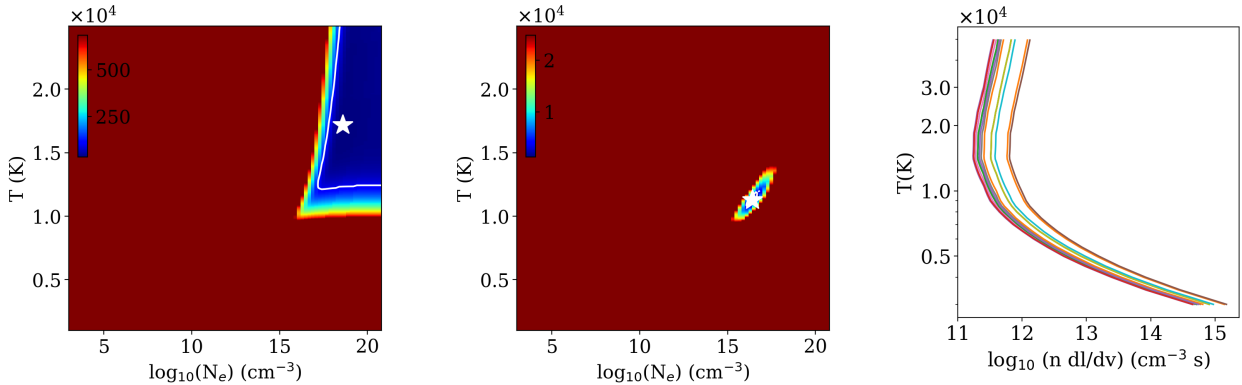


Figure 10. Results of the Saha equation and Sobolev LVG approximation analysis for the FeI/FeII lines identified in EX Lupi. From left to right: Saha results of fitting all 18 lines selected in velocity, Saha results of fitting 5 lines with high quality data and similar wavelengths, Sobolev results for the Fe II pair at 5316.6 and 5534.84 Å (each curve represents the theoretical values for the observed line ratio on a given observation date).

of-fit criteria. The resulting theoretical values for temperature and density-velocity gradient at the corresponding observed line ratios are shown. There is a shift in degenerate values across the observation dates, which may correspond to changes in the accretion, i.e. temperature changes. For the temperature to be consistent with the Saha results ($T \sim 1 - 1.5 \times 10^4$ K), this suggests a density-velocity gradient of $\sim 1 \times 10^{12}$ cm³ s. The fact that we do not observe other Fe lines with low A_{ki} (e.g. like those observed in ZCMa, Sicilia-Aguilar et al. 2020a) also concurs with a lower density.

The temperatures derived from the Fe lines are consistent with the higher end of what is expected in accretion shocks ($\sim 10,000$ K, Gullbring et al. 1998; Lima et al. 2010; Dodin & Lamzin 2012), also noting that the temperature is dependent on the size of the spot (Hartmann et al. 2016). Since the high densities and temperatures strongly suggest the possibility of non-LTE effects, the Sobolev LVG approximation would be more suitable in this case, since it does not depend on how the original level was populated. Nevertheless, as already pointed out by (Sicilia-Aguilar et al. 2015), some of the Fe lines are close to saturation, which would also impose a limitation.

The analysis of EX Lupi allows us to test the validity of the line finding algorithm, as well as to define the best strategy to analyse further sources and improve the line-finding strategy for lines with different properties. In addition to reproducing the previously inferred results, the new line velocity analysis of the extended dataset now available for EX Lupi, which covers twelve years of data from 2007 to 2019, with relatively dense sampling from 2009 to 2019, confirms the presence of a very well-localised and stable accretion-related spot on or very near the stellar surface proposed by Sicilia-Aguilar et al. (2015). The spot is relatively stable for even longer periods of time, despite the variations in the line strengths and accretion rate during those epochs. The confirmation of the rotational period of 7.417 d results in a corotation radius of 0.063 au, or between 8.5–9 R_* (considering the stellar radius estimate of 1.5–1.6 R_\odot , Sipos et al. 2009). This value is larger than the nominal 5 R_* typically assumed in accretion models (Gullbring et al. 1998), and it also means that the magnetospheric cavity in the inner disk of EX Lupi is larger than those typically assumed, being nearly as large as systems accreting in a propeller regime (e.g. LkCa 15 Donati et al. 2019). The line data can be saved to use them with a more complex (e.g. radiative transfer) models or fits.

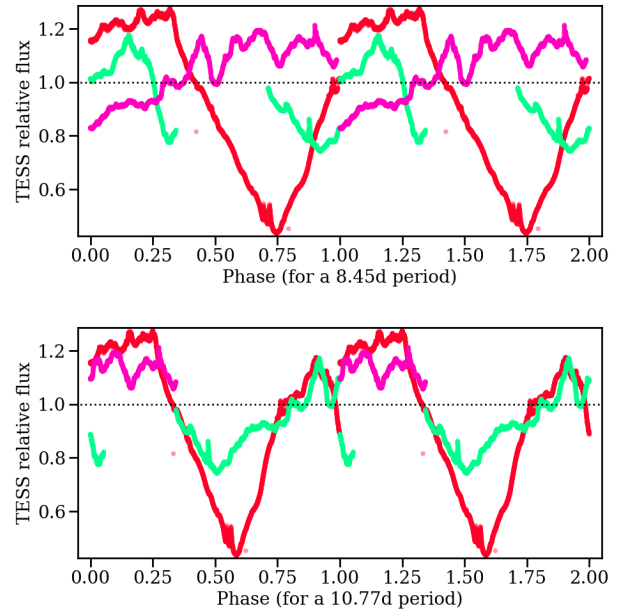


Figure 11. TESS normalised flux for GQ Lupi A, wrapped according to a 8.45d period (Broeg et al. 2007) (top) and according to a 10.77d period (bottom). The data are colour-coded according to different period cycles.

4.2 GQ Lupi A

GQ Lupi is a young K7 star (Herbig 1977; Donati et al. 2012) with a moderate accretion rate ($\dot{M} = 10^{-9} M_\odot/\text{yr}$, Frasca et al. 2017), mostly known for its wide-orbit companions (Neuhäuser et al. 2005; Alcalá et al. 2020), although for this part of the analysis we concentrate on the primary alone. Since the GQ Lupi b is about 6 mag fainter than GQ Lupi A (Neuhäuser et al. 2005), the photometry and spectroscopy are all dominated by the primary. The ESO archive contains a total of 76 spectra observed with HARPS (19 spectra), FEROS (39 spectra), and XSHOOTER (5 spectra each for the UVB and VIS arms, 8 spectra for the NIR arm) between 2005 and 2016, which make it an ideal target to test the capabilities of STAR-MELT for analysing and comparing multi-instrument, multi-epoch data. GQ Lupi A is known to have a rotational period of 8.5d and an inclination of 27 deg, as well as potential hot spots that trigger the

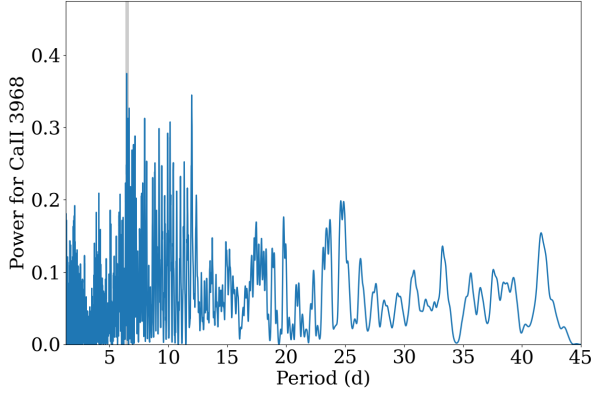


Figure 12. Example of the Lomb-Scargle periodogram for the Ca II 3968 Å line in GQ Lupi. Note that although there is a peak at 6.47 d, the strength of the peak results in a false-alarm probability of 2% for a white-noise model, and there are several other peaks similar in height.

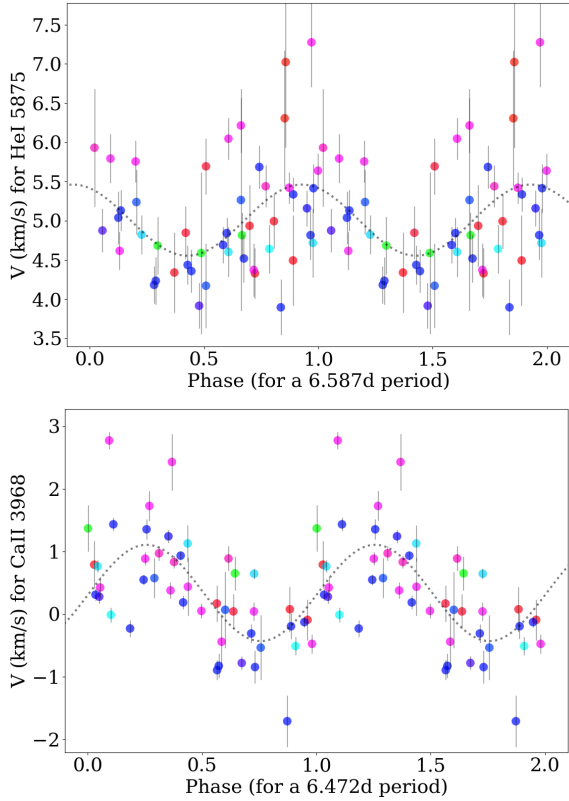


Figure 13. Tentative periods around 6–7 d observed for the line radial velocities in GQ Lupi A for He I 5875 Å (wrapped for a 6.587 d period) and Ca II 3934 Å (wrapped for a 6.472 d period). The colours indicate different period cycles, with the colour scale changing from red to purple from the first to the last MJD epoch.

observed photometric variability (Broeg et al. 2007; Donati et al. 2012). It also has a very strong and variable large-scale magnetic field (Donati et al. 2012).

The *TESS* data on GQ Lupi are inconclusive regarding periodicity (see Fig. 11). *TESS* reveals a large dip, similar to the variability pointed out by Broeg et al. (2007), but this dip is not observed on subsequent periods despite all observations being taken within a 25 d

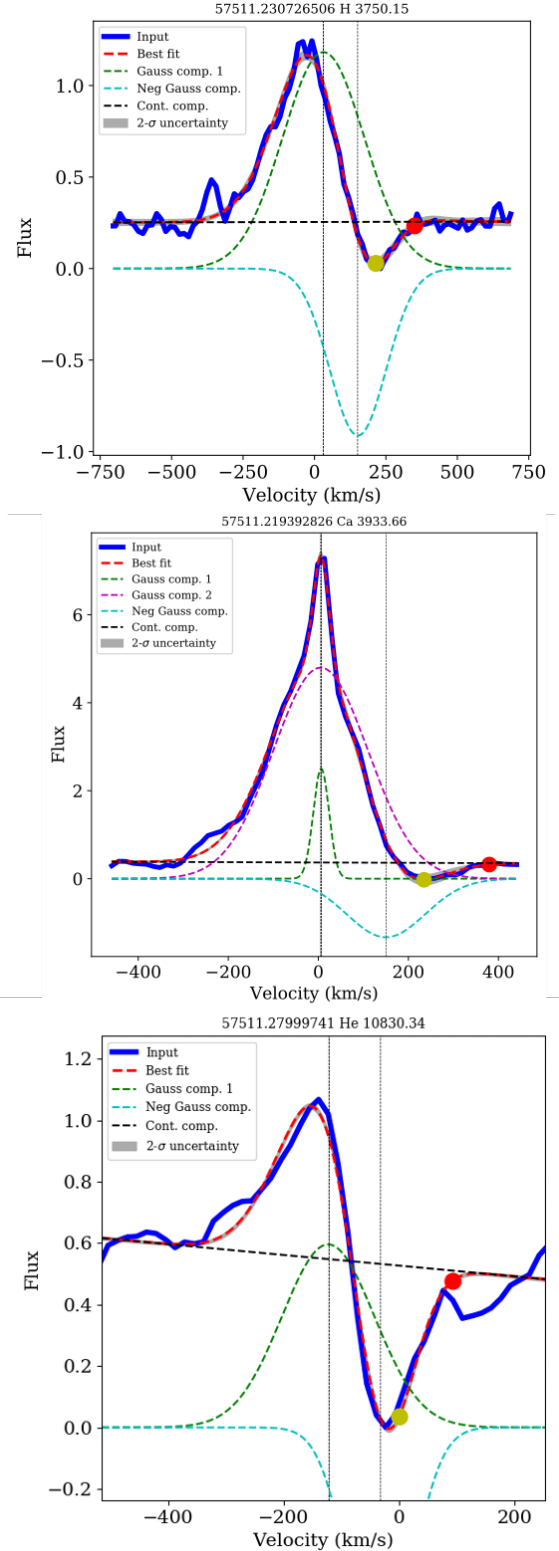


Figure 14. Example model fits of the XSHOOTER GQ Lupi A spectra for the H I 3750 Å (top) Ca II K 3934 Å (middle) and He I 10830 Å (bottom) lines. Each line displays a redshifted absorption component that is modelled by the negative Gaussian component. The positions of the maximum redshifted absorption velocity are indicated by the red circles, and the maximum absorption is marked by the yellow circles. The dotted vertical lines indicate the centre of the Gaussian components.

interval. This, together with the shape of the *TESS* lightcurve, suggests that the main cause for variations could be extinction events, which may be linked to the stellar rotation as it has been observed in other systems (Sicilia-Aguilar et al. 2020b). The best-fitting period for the *TESS* data is 10.77d, although the entire dataset covers less than 3 such periods so the result has a low significance. A secondary peak appears at 7.01d, but neither peak nor the ~ 8.5 d rotational period are conclusive.

A combination of the FEROS and HARPS data was used to estimate the rotational and radial velocity of the source, resulting in $V \sin i = 5.35 \pm 0.74$ km/s and $RV = -3.07 \pm 0.05$ km/s. Because most of the lines are relatively broad, fitting the continuum works best if we use a large under-sampling window and an order 3 polynomial. For the lower resolution XSHOOTER data, especially in the UV region, which is very rich in emission lines, a large under-sampling window (8\AA) is needed, and the best fit is obtained with an order 1 polynomial. Automated identification by STAR-MELT finds 9 lines in the combined HARPS and FEROS data, compared to 14 that are found in the same range of the XSHOOTER data (see Tab. D1). Both tend to miss $H\alpha$, $H\beta$, and $H\gamma$ because they are very broad and have deep central absorptions. The main difference lies in lines that are very weak and that become diluted by the higher resolution of FEROS and HARPS (such as the He II line at 4686\AA , or the He I line at 5015\AA). XSHOOTER reveals 41 lines, most of which are in the UV arm of the spectrum. The broad He I 10830\AA line is again a challenge for the automated detection due to its deep absorption. The conclusion is that, to extract such broad lines or lines that have central absorption components, the user may need to relax the typical matching range. In general, the $V \sin i$ is a good criterion to identify lines that are centrally peaked and not significantly red- or blue-shifted, but for stars like GQ Lupi, that show a variety of narrow and broad lines profiles, the best strategy is to extract them separately.

Looking at the emission lines extracted for the high-resolution FEROS and HARPS data, we detect a potential 6-7 d radial velocity modulation (Fig. 12). The modulation is most evident in the He I and Ca II lines. Other lines (including Fe I and He II) reveal low-significance (few per cent false-alarm probability for white-noise) modulations between 6-7d (see Fig. 13), which is suggestive of a quasi-period shorter than the nominal rotation period of 8.45 d. As observed for EX Lupi, the variations in the radial velocity of the lines do not exceed $V \sin i$ but the modulation is by far less clean. One of the reasons is that there are fewer datapoints and they are spread over a rather long timescale. Some lines, such as the He I 5875\AA , display redshifted profiles that may be an indication of wind absorption, so the interpretation of the periodicity is complicated, since it could include elements from the stellar rotation but also variability associated with the wind. In some cases, marginally-significant peaks arise at periods ~ 4 d, which could be caused if spots are found on the two sides of the star. Not all the lines show a sinusoidal profile, and the fact that some of the lines are not observed all the time may indicate that the line-emitting region is very rapidly changing or not always visible. This is all in agreement with the rapidly-changing complex signatures observed in the *TESS* lightcurve as well as with the rapid evolution of the spots and magnetic field structure (Donati et al. 2012). Rapid changes can explain why the modulation is, at best, quasi-periodic, and the false-alarm probability is never as low as observed for EX Lupi.

Although the radial velocity modulations of the lines are inconclusive in this case regarding the structure of the accretion structures, examination of the line profiles reveal that many of the lines display inverse PCygni or YY Ori-type profiles, with redshifted

absorptions that go below the continuum (see Fig. 14). Similar profiles had been observed at certain epochs in the past (Batalha et al. 2001), although in our case they appear to be always present in the XSHOOTER epochs. Redshifted absorptions are found in the higher Balmer lines, Ca II lines, and He I IR triplet lines. Many other lines (such as the Ca II IR triplet) have asymmetric profiles suggestive of redshifted absorption, although the absorption is not as marked and does not go below the continuum. Since this type of profile requires the accretion column to be observed along the line-of-sight, it is in agreement with the interpretation of the photometric variability as resulting from occultations by the disc material. Interestingly, because the inclination of the star has been estimated to be around 27° (Broeg et al. 2007; Donati et al. 2012), it would also indicate a misalignment between the inner and the outer disc. In fact, the outer disc has a significantly different inclination (60° ; MacGregor et al. 2017), which together with the system being a multiple stellar system, could lead to a complex and warped structure.

For the YY Ori-type profiles, the H I and He I profiles were fitted using STAR-MELT with a single positive and a negative Gaussian component, as well as the continuum linear component (Fig. 14). The Ca II-K line displays a defined narrow component in addition to the broad emission component and the redshifted absorption and was hence fitted with two positive Gaussians, the negative absorption Gaussian and the linear continuum component. The maximum redshifted absorption velocity, V_{red} , is calculated from the best fit model as the velocity at which the absorption correspond to 10% of the maximum absorption (Sicilia-Aguilar et al. 2017). Table 1 shows the observed V_{red} values obtained from this absorption profile fitting. Across all individual observations where this feature was well fitted, the mean values of V_{red} are 102 ± 12 , 313 ± 27 , and 390 ± 17 km/s for the He I, H I, and Ca II, respectively. We also tested the photospheric removed XSHOOTER spectra from ROTFIT (Frasca et al. 2017), to ensure that these absorption features were not distorted by the stellar photosphere. In each case, concurrent values of V_{red} were obtained from the ROTFIT reduced spectra.

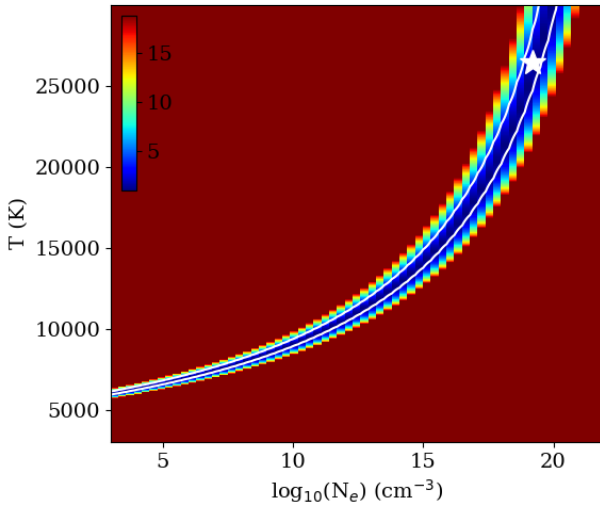
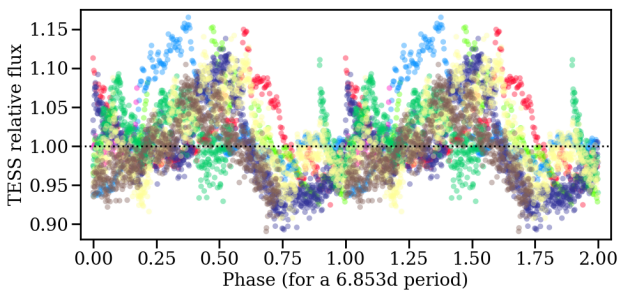
We find that V_{red} shows a significant anti-correlation with the total excitation energy of the transitions (E_k for the neutral lines and E_k plus ionisation potential energy for the Ca II lines). The highest infall velocities are reached by the lines produced in lower temperature regions, the same result we observed in ASASSN-13db (Sicilia-Aguilar et al. 2017), and opposite to the behaviour reported by Bertout et al. (1982) and Petrov et al. (2014b), for SCrA and CoD-35°10525. We note that we only use three species, whereas previous work has used many more metallic lines. It could therefore be that we are detecting an abundance difference between the H and He and the Ca, however, there is still difference in V_{red} values between the H and He. These lines also show variation in the V_{red} positions across the different observation dates, but with no clear correlation, nor enough data points to infer any periodicity.

Table 1 also shows the corresponding infall radii, calculated using the stellar parameters of $M_* = 1.05 M_\odot$, $R_* = 1.7 R_\odot$ and $i = 27^\circ$ (Donati et al. 2012) and assuming the material is in free-fall to the star. We assume that the infall is directed along the pole of the star and hence adjust the projected V_{red} by the inclination angle to achieve infall radii in this plane. These values do not account for possible complex geometries in the accretion column, but give an approximate value for the minimum infall radii. These values for the H and He are less than the nominal $5 R_*$ typically assumed for accretion, the Ca II is in good agreement.

We used the Saha equation to investigate the temperature and density ranges for the emitting regions. Figure 15 shows the results for four of the He lines identified in the GQ Lupi spectra: He I 4026,

Table 1. GQ Lupi maximum redshifted absorption velocity, V_{red} , for the YY Ori-type line profiles

Species/ λ (Å)	Excitation Energy (eV)	Mean V_{red} (km/s)	Infall Radius (R_*)
CaII 3934	9.26	390 ± 17	5.4
HI 3722	13.53	340 ± 12	2.6
HI 3750	13.50	341 ± 24	2.6
HI 3771	13.49	290 ± 7	1.8
HI 3798	13.46	326 ± 12	2.3
HI 3835	13.43	290 ± 18	1.8
HI 3889	13.39	293 ± 6	1.8
HeI 10830	20.96	102 ± 12	1.1

**Figure 15.** Saha results from the He I 4026, 4471, 5876 and He II 4686 lines in GQ Lupi, identified with STAR-MELT.**Figure 16.** TESS data for CVSO109, wrapped according to a 6.853d period. The data are colour-coded according to the different period cycles to better display the variations.

4471, 5876 Å and He II 4686 Å. The longer wavelength He lines are not included due to potential extinction affects and significantly different line profiles from these four lines. The median XSHOOTER spectra were used to determine the integrated flux ratios for the calculations. These results show similar densities and higher temperatures required for the He production than those shown for EX Lupi. As before, such high ionisation levels suggest non-thermal effects. The degenerate best-fit area is better constrained than for

the EX Lupi He lines, this may be because the line profile of the He II is more similar to the He I for GQ Lupi. The best-fit solution is dominated by this single He II line, while part of the He I emission may originate in a different location.

To summarise, for GQ Lupi A, STAR-MELT has allowed us to systematically extract detailed emission line results across many years of archival data. These analyses show a highly variable accreting system, with periodic and quasi-periodic rotational modulations in the emission lines consistent and semi-consistent with the observed photometric period. This is suggestive of spots on either side of the star, as well as non-constant magnetically channelled accretion along the line of sight, as shown by the inverse PCygni profiles; even in a system not so highly inclined. In this case, although the radial velocity signatures are inconclusive, the line profiles allow us to put an upper limit to the size of the magnetosphere, which is smaller than in the case of EX Lupi, and the line variability indicates that the accretion-related spots are very irregular in distribution and rapidly variable. Both findings show a stark contrast when compared to EX Lupi, although both stars have similar mass and age. In addition, the fact that the star has a low inclination while the disc and the accretion column seem more highly inclined suggests that there could be a star-disc, in addition to a star-magnetic field, misalignment.

4.3 CVSO109

CVSO109 (V* V462 Ori) is one of the ten *HST*/ULLYSES targets (Roman-Duval et al. 2020) located in the Orion OB1 association that was also observed by the ESO PENELLOPE large program (Manara et al. 2021). PENELLOPE is a contemporaneous survey to the *HST*/ULLYSES program and it is part of the ODYSSEUS¹⁴ collaboration (Outflows and Disks around Young Stars: Synergies for the Exploration of ULLYSES Spectra, Espaillat et al. in prep.), which will analyse the *HST*/ULLYSES YSO data and the connected ground-based data. In this work, we analyse the variability observed in CVSO109 from the four ESO VLT epochs to show what can be achieved with STAR-MELT across a shorter temporal coverage.

HST/ULLYSES observations revealed that CVSO109 is a binary that is unresolved in the ground based data (Proffitt et al. 2021). However, the secondary star has little to no excess emission (Espaillat et al. in prep.). Therefore, the emission lines we analyse here are all assumed to have originated from the primary, which is an accreting M0 CTT star (Ingleby et al. 2014, Espaillat et al. in prep.). The object has also been observed with *TESS* in sectors 6 and 32. *TESS* data, extracted using the principal component analysis (PCA) photometry tool to remove the systematics from nearby stars using the Python package ELEANOR (Feinstein et al. 2019; Brasseur et al. 2019), reveals a potential period around 6.853 d (see Fig. 16).

PENELLOPE observations were carried out across three nights with the ESO VLT instruments UVES and XSHOOTER (see Appendix B for instrument descriptions), with the XSHOOTER spectra being taken ~25 minutes before the final UVES epoch¹⁵. From the UVES spectra, we measure the projected rotational and radial velocities of the star as $V \sin i = 8.1 \pm 1.6$ and $RV = 16.76 \pm 0.21$ km/s. Lines were identified using a first order polynomial and a wavelength filter of 5 Å for the continuum subtraction. We identify 45 emission lines over a 3σ detection threshold. These lines were all identified using the NIST database (see Tab. D1), and 29 of them had been detected

¹⁴ <https://sites.bu.edu/odysseus/>

¹⁵ These final two epochs were near simultaneous to the *HST*/ULLYSES COS and STIS observations

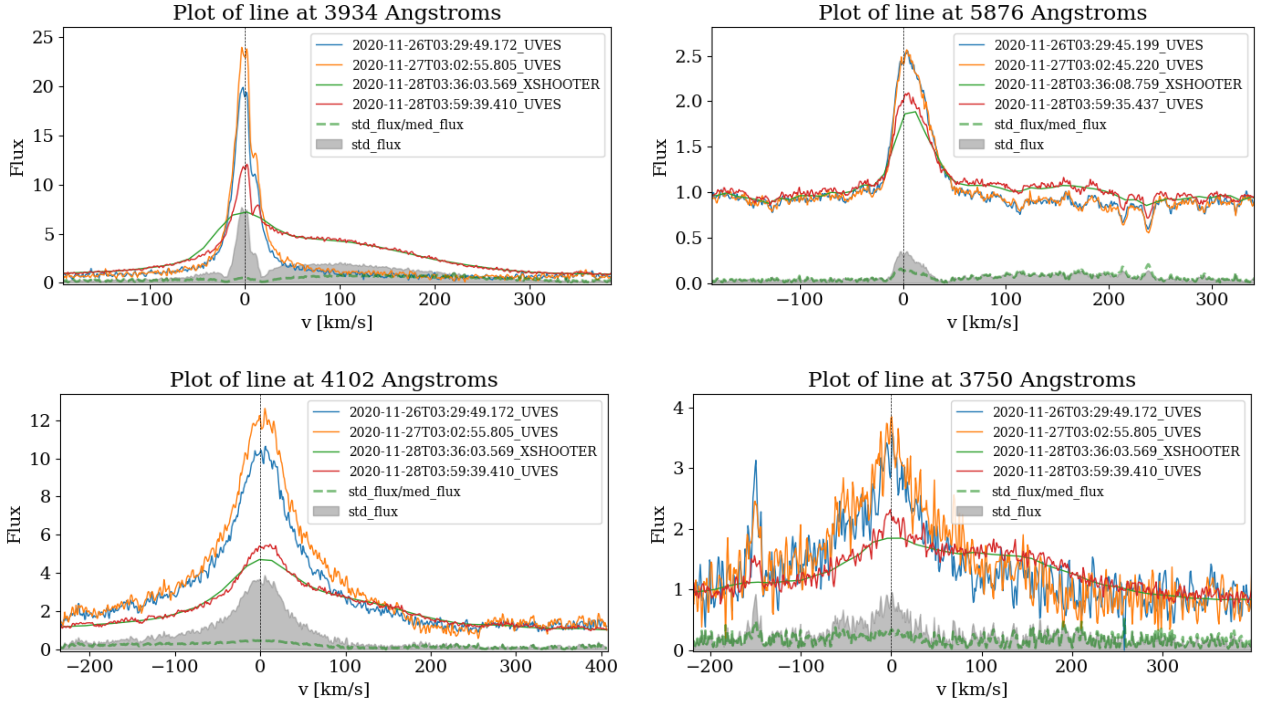


Figure 17. Variability plots of the redshifted emission wing in CVSO109 across the four epochs. Top left: Ca II K 3934 Å (model fit shown in Fig 18, top row), top right: He I 5876 Å bottom left: H I 4102 Å (model fit shown in Fig 18, bottom row), bottom right: H I 3750 Å.

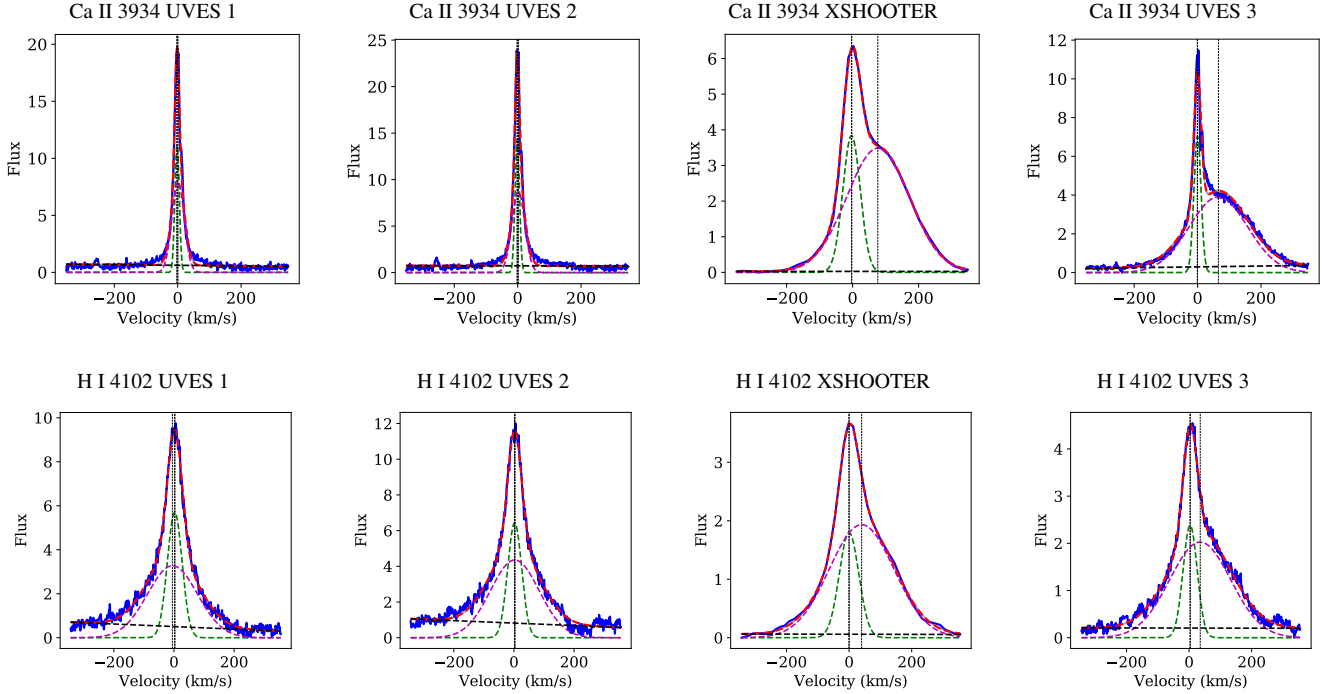


Figure 18. Model fits of the CVSO109 lines, input shown in blue, best fit shown in red. Top: Ca II K 3934 Å. Bottom: H I 4102 Å, each across the four epochs. In each instance, the line is fitted well by a broad and a narrow Gaussian components, indicated by the dashed lines. The redshifted emission wing can be clearly seen in the final two epochs.

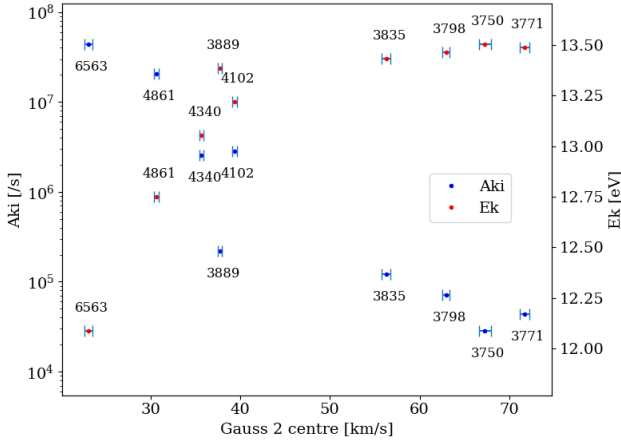


Figure 19. CVSO109 redshifted emission wing component central Gaussian velocity vs Ek and Aki for the well-fitted H lines in the XSHOOTER data. Error bars indicate the standard error in the Gaussian component centre value. Spearman’s Rank-Order Correlation coefficients of 0.96 ($p=2e-5$) and -0.93 ($p=2e-4$) are calculated for position and the Ek and Aki, respectively.

in our previous work in the spectra of EX Lupi, ASASSN-13db and ZCma (Sicilia-Aguilar et al. 2012, 2015, 2017, 2020a).

Many of the identified H and Ca II lines display a clear variability across the four epochs. Nine H lines, the Ca-K line and the Ca II IR triplet have a well-defined redshifted emission wing (see Figs. 17 and 18). The feature is also prominent in the Ca-H line, although blended with the adjacent H7 line, and in further H lines but with lower S/N. Figure 17 shows variability plots of the Ca II K 3934 Å He I 5876 Å H I 4102 Å and H I 3750 Å lines. The standard deviation can be used as a variability indicator, showing the redshifted wing feature clearly in the Ca II K line. The He I 5875 Å line also shows an extended redshifted component. The feature is not detected in other He lines.

This redshifted component is highly variable, being detected in the XSHOOTER and final UVES epoch taken with ~ 0.5 hr difference, but is absent from the first two UVES epochs, taken 1 and 2 days earlier. However, composite model fits of two Gaussians and a linear continuum to these lines both reveal the wing component structure, and still accurately model the first two UVES epochs as a narrow and broad component, but without the redshifted wing of the broad component. As with GQ Lupi A, we compared these model fits for the XSHOOTER data to the photosphere subtracted XSHOOTER spectra from ROTFIT (Manara et al. 2021). There was little change for the Balmer series and Ca II K lines. For these lines, the measured central Gaussian positions of the wing component from the ROTFIT spectra were within two standard errors of the original XSHOOTER spectra positions. The Ca II IR triplet lines from ROTFIT show a larger maximum flux, since the absorption component is accounted for, and the redshifted wing appears more defined. There is a difference of up to 10 km/s between the central Gaussian velocities of the ROTFIT and original XSHOOTER data for these IR lines. We note a difference in the $V \sin i$ from the value of 3.5 ± 1.1 km/s, calculated with the best veiling from ROTFIT (Manara et al. 2021). Other users of the package should be aware of this for stars with strong accretion. We will investigate line dependent veiling with STAR-MELT in future work.

Figure 18, top row, shows the model fits from each epoch for the Ca II K line and the bottom row shows the model fits to the H

I 4102 Å line. These model fits have a high accuracy for each of the epochs, with the H I 3750 Å line being the lowest S/N of the H Balmer lines still accurately fitted (in the XSHOOTER and one of the UVES epochs, the other lines listed are well-fitted across all four epochs). Table F1 shows the central position and FWHM of each Gaussian component, with standard errors from the model fits, for nine H I lines and the Ca II K line. The XSHOOTER fits to the Ca II IR triplet are also shown.

From the XSHOOTER fits, the wing components have centre Gaussian velocity ranges of ~ 20 -70 km/s for the H lines and ~ 75 -120 km/s in the Ca II K + IR triplet lines (see Tab. F1). The mean FWHM of these Gaussian components for the H and Ca K lines is 263 km/s with a standard deviation of 25 km/s, and for the Ca II IR lines the mean FWHM is 164 km/s with a standard deviation of 2 km/s. This suggests that the H I emission within the broad component is at a different location compared to the Ca II emission. The wing component central velocity from the H and Ca II K lines shows a blueshift between the XSHOOTER and final UVES epoch, across all observations except the H β line. There is also an observed redshift of the broad component central positions of these lines between the first two UVES epochs. These measured differences are clearly larger than the standard error of the Gaussian fits. If this broad component emission is due to rotating material, these results show that the maximum rotational velocity happens between the second UVES epoch and the XSHOOTER epoch, and that the material may have been at maximum blueshift \sim one-two days before the first UVES epoch.

Using the typical mass for an M0 star ($M_* \approx 0.55 M_\odot$, Siess et al. 2000), a stellar radius of $1.9 R_*$ (from the T and L_* , Manara et al. 2021), and an inclination of ~ 35 deg, which we calculate from the orbital period of 6.8 d and the measured $V \sin i$, we calculate upper limits for the radii of the material, assuming it is due to rotation. The mean observed emission wing velocities correspond to material producing emission at radii of ~ 2 and $11 R_*$ for the Ca II and H I lines, respectively; the opposite trend to that observed in GQ Lupi A for these species. These are still upper limits to the radii since although we consider the stellar inclination, what we observe during the XSHOOTER epoch is likely not at the maximum, as previously discussed. The co-rotation radius of this system is $\sim 6.5 R_*$, therefore infall contributions, especially from the Ca II, are also likely. Furthermore, using the lower inclination obtained from the ROTFIT $V \sin i$ also gives smaller radii, which is more suggestive of infall contributions to the overall motion if the material is in the orbital plane of the stellar rotation. Rapidly evolving velocity changes could result from a non-axisymmetric accretion structure or inner disc feature, similar to that identified from the spectra of EX Lupi (Sicilia-Aguilar et al. 2015, 2012). This may explain the dipper-like behaviour of the light curve, whereby the material in the disc is occulting the emission from the star. Without further data, we cannot confirm this, but the extrapolated timescale of this feature (if it is periodic) would also be consistent with the photometric period.

We further investigated the observed velocities in the H Balmer lines with respect to the transition properties of these lines. Figure 19 shows the the central position of the wing Gaussian component versus the transition probability (Aki) and excitation energy (Ek) for the H lines in the XSHOOTER spectra. There is a clear correlation between each parameter and the central position of the wing component. The material closest to the star has the lower transition probability and higher excitation energy. Spearman’s Rank-Order Correlation coefficients of 0.96 ($p=2e-5$) and -0.93 ($p=2e-4$) are calculated for position and the Ek and Aki, respectively. This result, together with the range in velocities across the epochs, not

only suggests that we are tracing rotating material at different radial locations, but also at different temperatures and densities at the varying distances. Although we do include the $H\alpha$ line because the measured standard error of the fit is relatively low, this line will be originating from many locations. This could be both accretion- and wind-related, and the wings could be strongly suppressed (Mendigutía et al. 2011). The H 3889 Å line appears to be a slight outlier in the plot. This line has more of a blueshift across the narrow components for all epochs; if we were to instead plot the broad component position minus the narrow component central position for all lines, this line then correlates better with the overall results. It is not clear why this line in particular shows this behaviour. The other lower velocity H lines still show the good correlation with the overall data between the central velocities and the transition properties.

These results from CVSO109 show that even with short temporal coverages, we are able to extract detailed information using STAR-MELT pertaining to variability and the geometry of accretion and inner disc structures. This is promising for further application to the rest of the PENELLOPE survey data, as well as other short time-scale spectral observations.

5 CONCLUSIONS & FUTURE WORK

This paper introduces the Python package STAR-MELT, which we have developed to analyse the stellar spectra of YSOs and apply the emission line tomography analysis. Data were analysed from UVES, XSHOOTER, FEROS, HARPS, and ESPaDoNs. STAR-MELT is also compatible with many further instruments, including ESPRESSO and SOPHIE. STAR-MELT can be run interactively within a Jupyter notebook, allowing for easy customisation, selections, and results that are compatible with other widely used Python libraries. The key capabilities of STAR-MELT were detailed within and include:

- Read in spectra data directly from the FITS files, with allowances for homogenization of data (accounting for barycentric corrections and flux scaling).
- Convenience functions of target and data selection, wavelength exclusions, and line plotting for both wavelength and velocity scales.
- RV and $V \sin i$ calculation using template stellar spectra (we plan to include synthetic model spectra for comparisons in a future version).
- Automatic emission line identification and matching to the NIST database of lines from the continuum subtracted spectra.
- Line fitting using Gaussian models. Customisable constraints may be applied to the centre/width of the Gaussian(s). χ^2 goodness-of-fit criteria applied.
- Periodicity analysis using periodograms and phase folded variability plots.
- Physical property approximations using Saha/Boltzmann equations and the Sobolev large velocity gradient approximation.

In addition to detailing the STAR-MELT package functionality, we also presented its application to three PMS stars, EX Lupi, GQ Lupi A and CVSO109.

The EX Lupi quiescence data from 2007-2019 were used to confirm that STAR-MELT produces the same results that we found in our previous work on this star (Kóspál et al. 2014; Sicilia-Aguilar et al. 2015). All previously identified strong lines were recovered and well-fitted. As were the periodicities and offset in phase between the highly energetic lines, such as the He II and Fe lines and the lower energy lines such as the Mg I. Line emission from He I and He II is

consistent with very high temperature (over 20,000K) and density, indicative of a small spot size and non-thermal ionisation that will require a more detailed treatment in the future. The temperature derived from Fe I/Fe II lines is significantly lower.

GQ Lupi A displays inverse PCygni YY-Ori type profiles in many of the H , He and Ca II lines. Accurate model fitting to these data reveal the maximum position of the infall velocity is anti-correlated with the excitation energy, suggesting that the highest velocities are achieved by lines produced in the lowest temperature regions. There is also suggestion of a misalignment between the stellar and disc rotation axes. The infall velocities allow us to put an upper limit on the size of the magnetosphere, which is smaller than the one observed in EX Lupi.

CVSO109 is the first of the PENELLOPE survey (Manara et al. 2021) targets to be analysed by STAR-MELT. Clear variability is observed across the four epochs by a redshifted emission wing in the H and Ca II lines. The central position of this emission wing correlates with the transition probability and upper-energy level of the lines. Such a feature is indicative of rotating material, which we show may span a range of radial locations with different temperatures.

By using as examples stars with different amounts of data and time sampling, we also reveal that important constraints to the accretion properties and associated structures can be placed even with incomplete time coverage, if the multiple emission lines observed are accurately extracted and fitted. Although the three stars examined here are similar in age and stellar mass, we also find a variety of behaviours regarding variability and stability of accretion structures as well as sizes of the magnetospheres (upper limits of ~ 9 , 5, and 6 R_* for EX Lupi, GQ Lupi A and CVSO109, respectively). This may indicate differences in the stellar structure and/or in the properties of the inner disc, including differences in the star-disc inclination and in the magnetic field topology (Johnstone et al. 2014). The analysis of the line variability reveals that EX Lupi is accreting in a very stable mode, while GQ Lupi has unstable accretion (Kurosawa & Romanova 2013) and may display a misalignment between the inner and outer disc and/or the disc and accretion channels. Further data are required for confirmation of the nature of the variability in CVSO109, but our results show good evidence for periodic rotating material with infall contributions, which may be occulting the star. This also suggests that material at high latitude, crossing the line-of-sight may be more common than previously thought, being observed in stars that are not highly inclined.

STAR-MELT automates many aspects of our analysis procedure, allowing for systematic results to be obtained quickly. However, line identification remains a complex process, requiring careful examination of the results obtained. This paper has shown that we can effectively use STAR-MELT to facilitate our analysis of time-resolved spectra of PMS stars; with many further applications for emission line analysis. For example, we are currently using STAR-MELT to identify and analyse emission lines from hyper-velocity impact flash spectra (Spathis et al. 2021), as well as time- and spatially-resolved coronal mass ejections from solar data.

STAR-MELT is available to the community on [GitHub](#) and the example notebook can be run online via the [binder platform](#).

ACKNOWLEDGEMENTS

We thank the anonymous referee for their useful comments and suggestions that have improved this work. JCW, ASA and SM are supported by the STFC grant number ST/S000399/1 ("The Planet-

Disk Connection: Accretion, Disk Structure, and Planet Formation"). This work benefited from discussions with the ODYSSEUS team (HST AR-16129), <https://sites.bu.edu/odysseus/>. This project has received funding from the European Union's Horizon 2020 research and innovation programme under the Marie Skłodowska-Curie grant agreement No 823823 (DUSTBUSTERS). This research received financial support from the project PRIN-INAF 2019 "Spectroscopically Tracing the Disk Dispersal Evolution". We also thank the ESO Data Archive Helpdesk and, in particular, John Pritchard, for their valuable help.

DATA AVAILABILITY

All spectral data used in this work are publicly available. Data for EX Lupi and GQ Lupi A are accessed from the ESO archive (<http://archive.eso.org/>). Data for CVSO109 from the ESO PENELLOPE survey are available within the ODYSSEUS repository at <https://doi.org/10.5281/zenodo.4477091> for the XSHOOTER data and <https://doi.org/10.5281/zenodo.4478360> for the UVES data. The STAR-MELT package is available at https://github.com/justyncw/STAR_MELT. The authors also welcome collaborative projects using the package.

REFERENCES

- Alcalá J. M., et al., 2014, *A&A*, 561, A2
- Alcalá J. M., et al., 2017, *A&A*, 600, A20
- Alcalá J. M., et al., 2020, arXiv:2001.10879 [astro-ph]
- Andrews S. M., et al., 2016, *ApJ*, 820, L40
- Andrews S. M., et al., 2018, *ApJ*, 869, L41
- Antonucci S., et al., 2017, *A&A*, 606, A48
- Aspin C., Reipurth B., Herczeg G. J., Capak P., 2010, *ApJ*, 719, L50
- Astropy Collaboration et al., 2013, *A&A*, 558, A33
- Astropy Collaboration et al., 2018, *aj*, 156, 123
- Ballester P., Modigliani A., Boitquin O., Cristiani S., Hanuschik R., Kaufer A., Wolf S., 2000, *The Messenger*, 101, 31
- Batalha C., Lopes D. F., Batalha N. M., 2001, *ApJ*, 548, 377
- Beristain G., 2000, PhD Thesis, UNIVERSITY OF MASSACHUSETTS
- Beristain G., Edwards S., Kwan J., 1998, *ApJ*, 499, 828
- Bertout C., Wolf B., Carrasco L., Mundt R., 1982, *A&AS*, 47, 419
- Bouvier J., Covino E., Kovo O., Martin E. L., Matthews J. M., Terranegra L., Beck S. C., 1995, *A&A*, 299, 89
- Bouvier J., Alencar S. H. P., Harries T. J., Johns-Krull C. M., Romanova M. M., 2007, in Reipurth B., Jewitt D., Keil K., eds, *Protostars and Planets V*. p. 479
- Brasseur C. E., Phillip C., Fleming S. W., Mullally S. E., White R. L., 2019, *Astrocute: Tools for creating cutouts of TESS images* (ascl:1905.007)
- Broeg C., Schmidt T. O. B., Guenther E., Gaedke A., Bedalov A., Neuhauser R., Walter F. M., 2007, *A&A*, 468, 1039
- Buder S., et al., 2019, *A&A*, 624, A19
- Busà I., Pagano I., Rodonò M., Neff J. E., Lanzafame A. C., 1999, *A&A*, 350, 571
- Cauley P. W., Johns-Krull C. M., Hamilton C. M., Lockhart K., 2012, *The Astrophysical Journal*, 756, 68
- Crockett C. J., Mahmud N. I., Prato L., Johns-Krull C. M., Jaffe D. T., Hartigan P. M., Beichman C. A., 2012, *The Astrophysical Journal*, 761, 164
- Curcio J. A., Drummeter L. F., Knestrick G. L., 1964, *Appl. Opt.*, 3, 1401
- Czesla S., Schröter S., Schneider C. P., Huber K. F., Pfeifer F., Andreasen D. T., Zechmeister M., 2019, PyA: Python astronomy-related packages
- Dekker H., D'Odorico S., Kaufer A., Delabre B., Kotzłowski H., 2000, in Iye M., Moorwood A. F., eds, *Society of Photo-Optical Instrumentation Engineers (SPIE) Conference Series Vol. 4008, Optical and IR Telescope Instrumentation and Detectors*. pp 534–545, doi:10.1117/12.395512
- Dodin A. V., Lamzin S. A., 2012, *Astronomy Letters*, 38, 649
- Donati J. F., et al., 2012, *MNRAS*, 425, 2948
- Donati J. F., et al., 2019, arXiv:1911.12818 [astro-ph]
- Dupree A. K., et al., 2012, *ApJ*, 750, 73
- Evans D. S., 1967, *The Revision of the General Catalogue of Radial Velocities*. Vol. 30
- Famaey B., Jorissen A., Luri X., Mayor M., Udry S., Dejonghe H., Turon C., 2005, *A&A*, 430, 165
- Fang M., van Boekel R., Wang W., Carmona A., Sicilia-Aguilar A., Henning T., 2009, *Astronomy and Astrophysics*, 504, 461
- Fang M., Sicilia-Aguilar A., Roccatagliata V., Fedele D., Henning T., Eiroa C., Müller A., 2014, *A&A*, 570, A118
- Feinstein A. D., et al., 2019, *PASP*, 131, 094502
- Frasca A., Alcalá J. M., Covino E., Catalano S., Marilli E., Paladino R., 2003, *A&A*, 405, 149
- Frasca A., Guillout P., Marilli E., Freire Ferrero R., Biazio K., Klutsch A., 2006, *A&A*, 454, 301
- Frasca A., Kovári Z., Strassmeier K. G., Biazio K., 2008, *A&A*, 481, 229
- Frasca A., Biazio K., Alcalá J. M., Manara C. F., Stelzer B., Covino E., Antonucci S., 2017, *A&A*, 602, A33
- Freudling W., Romaniello M., Bramich D. M., Ballester P., Forchi V., García-Dabó C. E., Moehler S., Neeser M. J., 2013, *A&A*, 559, A96
- Gallet F., Bolmont E., Mathis S., Charbonnel C., Amard L., 2017, *A&A*, 604, A112
- Giannini T., et al., 2013, *ApJ*, 778, 71
- Ginsburg A., et al., 2019, *AJ*, 157, 98
- Gontcharov G. A., 2006, *Astronomy Letters*, 32, 759
- Gravity Collaboration et al., 2019, *A&A*, 632, A53
- Gullbring E., Hartmann L., Briceño C., Calvet N., 1998, *ApJ*, 492, 323
- Hamann F., 1994, *ApJS*, 93, 485
- Hamann F., Persson S. E., 1992a, *ApJS*, 82, 247
- Hamann F., Persson S. E., 1992b, *ApJS*, 82, 285
- Hartmann L., Herczeg G., Calvet N., 2016, *Annual Review of Astronomy and Astrophysics*, 54, 135
- Herbig G. H., 1977, *ApJ*, 214, 747
- Herbig G. H., 2007, *AJ*, 133, 2679
- Herbig G. H., 2008, *AJ*, 135, 637
- Herbig G. H., Aspin C., Gilmore A. C., Imhoff C. L., Jones A. F., 2001, *PASP*, 113, 1547
- Herbst W., Bailer-Jones C. A. L., Mundt R., Meisenheimer K., Wackermann R., 2002, *Astronomy and Astrophysics*, 396, 513
- Herczeg G. J., Cruz K. L., Hillenbrand L. A., 2009, *The Astrophysical Journal*, 696, 1589
- Hojjatpanah S., et al., 2019, *A&A*, 629, A80
- Hubeny I., Mihalas D., 2014, *Theory of Stellar Atmospheres*
- Ingleby L., Calvet N., Hernández J., Hartmann L., Briceño C., Miller J., Espaillat C., McClure M., 2014, *ApJ*, 790, 47
- Johns-Krull C. M., et al., 2016, *ApJ*, 826, 206
- Johnstone C. P., Jardine M., Gregory S. G., Donati J. F., Hussain G., 2014, *MNRAS*, 437, 3202
- Jones A. F. A. L., 2008, *Central Bureau Electronic Telegrams*, 1217, 1
- Joy A. H., 1945, *ApJ*, 102, 168
- Kanagawa K. D., Tanaka H., Szuszkiewicz E., 2018, *ApJ*, 861, 140
- Kaufer A., Stahl O., Tubbesing S., Nørregaard P., Avila G., Francois P., Pasquini L., Pizzella A., 1999, *The Messenger*, 95, 8
- Kellerer D. E., et al., 1999, in Carruthers G. R., Dymond K. F., eds, *Society of Photo-Optical Instrumentation Engineers (SPIE) Conference Series Vol. 3818, Ultraviolet Atmospheric and Space Remote Sensing: Methods and Instrumentation II*. pp 170–179, doi:10/cz3sf9
- Kóspál Á., et al., 2014, *Astronomy and Astrophysics*, 561, A61
- Kramida, A. Ralchenko, Yu. Reader, J. and NIST ASD Team 2020. , doi:https://doi.org/10.18434/T4W30F
- Kurosawa R., Romanova M. M., 2013, *MNRAS*, 431, 2673
- Lehmann T., Reipurth B., Brandner W., 1995, *A&A*, 300, L9
- Lima G. H. R. A., Alencar S. H. P., Calvet N., Hartmann L., Muzerolle J., 2010, *A&A*, 522, A104
- Lin D. N. C., Bodenheimer P., Richardson D. C., 1996, *Nature*, 380, 606
- Lynden-Bell D., Pringle J. E., 1974, *MNRAS*, 168, 603

MacGregor M. A., et al., 2017, *ApJ*, **835**, 17

Manara C. F., et al., 2021, *A&A*, **650**, A196

Marsh T. R., Horne K., 1988, *MNRAS*, **235**, 269

Matt S. P., MacGregor K. B., Pinsonneault M. H., Greene T. P., 2012, *The Astrophysical Journal Letters*, **754**, L26

Mayor M., et al., 2003, *The Messenger*, **114**, 20

McGinnis P., Bouvier J., Gallet F., 2020, *Monthly Notices of the Royal Astronomical Society*, **497**, 2142

Mendigutía I., Calvet N., Montesinos B., Mora A., Muzerolle J., Eiroa C., Oudmaijer R. D., Merín B., 2011, *A&A*, **535**, A99

Mihalas D., 1978, *Stellar Atmospheres*. Astronomy and Astrophysics Series, W. H. Freeman, <https://books.google.co.uk/books?id=P197QgAACAAJ>

Modigliani A., et al., 2010, in Silva D. R., Peck A. B., Soifer B. T., eds, *Society of Photo-Optical Instrumentation Engineers (SPIE) Conference Series Vol. 7737, Observatory Operations: Strategies, Processes, and Systems III*. p. 773728, doi:10.1117/12.857211

Molenda-Žakowicz J., et al., 2013, *MNRAS*, **434**, 1422

Mora A., et al., 2004, *A&A*, **419**, 225

Morbidelli A., Raymond S. N., 2016, *Journal of Geophysical Research (Planets)*, **121**, 1962

Müller A., et al., 2013, *A&A*, **556**, A3

Neff J. E., Walter F. M., Rodono M., Linsky J. L., 1989, *A&A*, **215**, 79

Neuhäuser R., Guenther E. W., Wuchterl G., Mugrauer M., Bedalov A., Hauschildt P. H., 2005, *A&A*, **435**, L13

Newville M., Stensitzki T., Allen D. B., Ingargiola A., 2014, *LM-FIT: Non-Linear Least-Square Minimization and Curve-Fitting for Python*, doi:10.5281/zenodo.11813, <https://doi.org/10.5281/zenodo.11813>

Paardekooper S.-J., Baruteau C., Kley W., 2011, *MNRAS*, **410**, 293

Petrov P. P., Kurosawa R., Romanova M. M., Gameiro J. F., Fernandez M., Babina E. V., Artemenko S. A., 2014a, *MNRAS*, **442**, 3643

Petrov P. P., Gahm G. F., Herczeg G. J., Stempels H. C., Walter F. M., 2014b, *A&A*, **568**, L10

Proffitt C. R., et al., 2021, *Research Notes of the American Astronomical Society*, **5**, 36

Ralchenko Y., et al., 2005, in Kato T., Kato D., Funaba H., eds, *American Institute of Physics Conference Series Vol. 771, Atomic and Molecular Data and their Applications*. pp 276–285, doi:10/ffs6mj

Roman-Duval J., et al., 2020, *Research Notes of the American Astronomical Society*, **4**, 205

Savitzky A., Golay M. J. E., 1964, *Analytical Chemistry*, **36**, 1627

Schneider P. C., Manara C. F., Facchini S., Günther H. M., Herczeg G. J., Fedele D., Teixeira P. S., 2018, *A&A*, **614**, A108

Shu F. H., Najita J., Ruden S. P., Lizano S., 1994, *The Astrophysical Journal*, **429**, 797

Sicilia-Aguilar A., et al., 2012, *A&A*, **544**, A93

Sicilia-Aguilar A., Fang M., Roccatagliata V., Collier Cameron A., Kóspál Á., Henning T., Ábrahám P., Sipos N., 2015, *A&A*, **580**, A82

Sicilia-Aguilar A., et al., 2016, *Publications of the Astronomical Society of Australia*, **33**, e059

Sicilia-Aguilar A., et al., 2017, *Astronomy and Astrophysics*, **607**, A127

Sicilia-Aguilar A., Bouvier J., Dougados C., Grankin K., Donati J.-F., 2020a, arXiv:2008.13678 [astro-ph]

Sicilia-Aguilar A., Manara C. F., de Boer J., Benisty M., Pinilla P., Bouvier J., 2020b, *A&A*, **633**, A37

Siess L., Dufour E., Forestini M., 2000, *A&A*, **358**, 593

Sipos N., Ábrahám P., Acosta-Pulido J., Juhász A., Kóspál Á., Kun M., Moór A., Setiawan J., 2009, *A&A*, **507**, 881

Soubiran C., et al., 2018, *A&A*, **616**, A7

Spathis V., Price M. C., Tandy J. D., Wozniakiewicz P. J., Campbell-White J., Sicilia-Aguilar A., 2021, in *Lunar and Planetary Science Conference. Lunar and Planetary Science Conference*. p. 1625

Tanaka H., Takeuchi T., Ward W. R., 2002, *ApJ*, **565**, 1257

Valenti J. A., Fischer D. A., 2005, *ApJS*, **159**, 141

Vernet J., et al., 2011, *A&A*, **536**, A105

Vioque M., Oudmaijer R. D., Baines D., Mendigutía I., Pérez-Martínez R., 2018, *A&A*, **620**, A128

Table A1. List of standard stars used for the RV and $V \sin i$ calculations.

Star	Sp Type	RV [km/s]	Reference
* tau Sco	B0.2V	2.0 ± 0.9	Evans (1967)
* alf Leo	B8IVn	5.9 ± 2.0	Evans (1967)
HD 18331	A1V	-10.7 ± 0.9	Gontcharov (2006)
* alf PsA	A4V	6.5 ± 0.5	Gontcharov (2006)
* alf CMi	F5IV	-15.9 ± 0.1	Buder et al. (2019)
* alf Cen A	G2V	-21.4 ± 0.8	Valenti & Fischer (2005)
* tau Cet	G8V	-16.6	Soubiran et al. (2018)
* 70 Oph	K0V	-5.8	Soubiran et al. (2018)
HD 114386	K3V	33.4	Soubiran et al. (2018)
GJ488	M0V	5.0	Hojjatpanah et al. (2019)
* alf Cet	M1.5IIIa	-26.1	Famaey et al. (2005)
* psi Phe	M4III	2.9 ± 1.5	Gontcharov (2006)

Williams J. P., Cieza L. A., 2011, *ARA&A*, **49**, 67

APPENDIX A: STANDARD STARS FOR RV AND $V \sin i$ CALCULATION

APPENDIX B: INSTRUMENT DESCRIPTIONS

This section contains technical descriptions of the instruments used to obtain the data for this work.

B1 FEROS and HARPS

The ESO La Silla instruments FEROS (Fiber-fed Extended Range Optical Spectrograph; Kaufer et al. 1999) has a resolution of $R = 48000$, and a wavelength coverage between 3500–9200 Å, containing in total 39 echelle orders. HARPS (High Accuracy Radial velocity Planet Searcher; Mayor et al. 2003) has a higher resolution of $R = 115000$, and a lower spectral coverage of 3780–6910 Å. Data were taken from the ESO Science Archive and had been reduced by the standard pipelines. Since the majority of the 1-dimensional spectral data on the ESO Science Archive now follows the ESO Science Data Products (SDP) standard, STAR-MELT was designed to be fully conformative with this standard. We incorporate an adapted version of the ESO python script `1DSPECTRUM.PY`, version: 2017-08-07 available at

<https://archive.eso.org/cms/eso-data/help/1dspectra.html#Python>, to extract the 1-D spectrum data from the FITS files. Further modifications also allow for other ESO and non-ESO instruments to be read in directly.

B2 UVES and XSHOOTER

The ESO VLT instrument UVES (Ultraviolet and Visual Echelle Spectrograph Dekker et al. 2000) uses a single long slit, dividing the spectra in two arms, Red (480 nm) and Blue (450 nm). The 0.6'' wide slits in both arms were used for these observations, leading to a spectral resolution $R \sim 70,000$. The wavelength ranges of 330–450 nm, 480–575 nm, and 585–680 nm were simultaneously covered. For the data in this work, the exposure times allowed for S/N at 630 nm of at least 50 in each observation.

The ESO VLT instrument XSHOOTER (Vernet et al. 2011) is a slit-fed (11'' long) spectrograph, providing simultaneous coverage of the wavelength region between ~ 300 nm and ~ 2500 nm, divided into three arms, UVB ($300 \leq \lambda \leq 500$ nm), VIS ($500 \leq \lambda \leq 1000$ nm), and NIR ($1000 \leq \lambda \leq 2500$ nm). Exposures with a set of a 1.0''–0.4''–0.4'' wide slits for the UVB, VIS, and NIR arms,

Table C1. Summary of observations used.

Star/ Programme ID	Instrument	Obs. Start Date	# Obs.
EX Lupi			
079.A-9017	FEROS	2007-07-29T03:45:21	3
082.C-0390	HARPS	2009-02-12T08:06:05	5
082.C-0427	HARPS	2009-03-01T07:12:24	4
083.A-9011	FEROS	2009-08-13T00:55:13	3
083.A-9017	FEROS	2009-09-02T00:51:49	1
084.A-9011	FEROS	2010-03-02T07:39:24	4
085.A-9027	FEROS	2010-04-23T09:27:19	15
086.A-9006	FEROS	2011-01-25T08:54:32	3
086.A-9012	FEROS	2011-03-10T07:33:59	3
087.A-9013	FEROS	2011-04-17T04:33:53	8
089.A-9007	FEROS	2012-07-03T00:19:10	10
091.A-9013	FEROS	2013-07-15T23:16:04	14
092.A-9007	FEROS	2014-02-16T06:47:50	17
16AF03	ESPaDOnS	2016-06-09T09:00:00	50
099.A-9010	FEROS	2017-06-07T03:15:27	4
19AF50	ESPaDOnS	2019-05-31T09:56:09	24
GQ Lupi			
074.C-0037	HARPS	2005-02-06T08:43:33	7
075.C-0710	HARPS	2005-05-05T01:10:18	9
079.A-9009	FEROS	2007-05-05T05:41:06	3
081.A-9005	FEROS	2008-04-18T03:28:44	2
081.A-9023	FEROS	2008-06-16T06:23:08	3
082.C-0390	HARPS	2009-02-12T08:20:46	3
083.A-9004	FEROS	2009-04-22T07:37:29	14
083.A-9011	FEROS	2009-08-11T00:18:23	1
083.A-9017	FEROS	2009-06-09T05:55:37	2
085.C-0764	XSHOOTER	2010-05-05T06:16:33	3
085.A-9027	FEROS	2010-05-24T05:08:24	14
097.C-0669	XSHOOTER	2016-05-03T05:15:55	15
CVSO 109			
106.20Z8.009	UVES	2020-11-26T03:29:45	3
106.20Z8.002	XSHOOTER	2020-11-28T03:36:03	1

respectively, allows for high S/N spectra with $R \sim 5400$, 18400, and 11600 in the three arms, respectively. The exposure times were such that the S/N at 400 nm is about $\gtrsim 3$ -5 and in the VIS and NIR arms $\gtrsim 100$.

Data reduction for the data acquired with each instrument is done using the ESO Reflex workflow v2.8.5 (Freudling et al. 2013), using the pipeline for each instruments: the UVES v6.1.3 pipeline (Ballester et al. 2000), the XSHOOTER pipeline v3.5.0 (Modigliani et al. 2010), as described by Manara et al. (2021). The pipelines apply the standard flat, bias, and dark correction, wavelength calibration, spectral rectification and extraction of the 1D spectrum.

B3 ESPaDOnS

The CFHT instrument ESPaDOnS: an Echelle SpectroPolarimetric Device for the Observation of Stars is a fibre-fed echelle spectropolarimeter with a spectral resolution $R = 65000$, and a wavelength coverage between 3700-10500Å, over 40 echelle orders. This work only features the spectral intensity (Stokes I) data, which was obtained from the CHFT archive and has been reduced with the standard pipeline.

APPENDIX C: OBSERVATION LOG

APPENDIX D: LIST OF IDENTIFIED LINES

Included in the supplementary material of the article.

Table D1: List of lines identified in EX Lupi, CVSO 109, GQ Lupi A. Previous ID column corresponds to lines identified in our previous work. o: outburst, q: quiescence. E12,E15: EX Lupi (Sicilia-Aguilar et al. 2012, 2015), A17: ASASSN-13db (Sicilia-Aguilar et al. 2017), Z20: ZCma (Sicilia-Aguilar et al. 2020a). Wavelengths marked by * indicate possible blends or multiple matches to the identified line. Acc denotes the accuracy for each transition strength from the NIST database, ranging from $\leq 0.3\%$ for AAA to $> 50\%$ for E.

λ (Å)	Element	Aki [s]	Acc	Ei [eV]	Ek [eV]	Previous ID	Star
3119.49	Fe I	8.3e+06	B	2.43	6.41		CVSO 109
3192.06*	Fe II	5.0e+05	D	3.81	7.70		CVSO 109
3192.27*	Ti II	2.2e+06	B'	1.08	4.96		CVSO 109
3227.74*	Fe II	8.9e+06	C	1.67	5.51		CVSO 109/GQ Lupi
3227.80*	Fe I	5.0e+07	B	2.43	6.27		CVSO 109/GQ Lupi
3255.89	Fe II	2.8e+05	B	0.99	4.79		CVSO 109/GQ Lupi
3277.35	Fe II	3.3e+05	B	0.99	4.77		CVSO 109/GQ Lupi
3278.92	Ti II	8.8e+07	B+	1.08	4.86		CVSO 109
3387.83	Ti II	2.8e+07	B+	0.03	3.69		CVSO 109
3483.01	Fe I	1.4e+05	B	0.91	4.47		CVSO 109
3691.56	H I	3.7e+03	AAA	10.20	13.56		GQ Lupi
3697.16	H I	4.9e+03	AAA	10.20	13.55		GQ Lupi
3703.86	H I	6.7e+03	AAA	10.20	13.55		GQ Lupi
3711.98	H I	9.2e+03	AAA	10.20	13.54	Z20o	GQ Lupi
3721.94	H I	1.3e+04	AAA	10.20	13.53		CVSO 109/GQ Lupi
3734.37	H I	1.9e+04	AAA	10.20	13.52		CVSO 109/GQ Lupi
3736.90	Ca II	1.7e+08	C	3.15	6.47	Z20o	CVSO 109
3750.15	H I	2.8e+04	AAA	10.20	13.50	Z20o	CVSO 109/GQ Lupi
3761.32*	Ti II	1.2e+08	A'	0.57	3.87	Z20o	CVSO 109
3761.41*	Fe I	1.0e+06	B	2.59	5.88	Z20o	CVSO 109
3770.63	H I	4.4e+04	AAA	10.20	13.49	Z20o	CVSO 109/GQ Lupi
3797.91	H I	7.1e+04	AAA	10.20	13.46	Z20o	CVSO 109/GQ Lupi
3825.88	Fe I	6.0e+07	A	0.91	4.15		CVSO 109
3835.40	H I	1.2e+05	AAA	10.20	13.43	Z20o/E12q	CVSO 109/GQ Lupi
3889.06	H I	2.2e+05	AAA	10.20	13.39	Z20o/E12q	CVSO 109/GQ Lupi
3933.66	Ca II	1.5e+08	C	0.00	3.15	Z20q/Z20o/E12q	CVSO 109/GQ Lupi/EX Lupi
3968.47	Ca II	1.4e+08	C	0.00	3.12	Z20o/E12q	CVSO 109/GQ Lupi/EX Lupi
3970.04	H I	4.4e+05	AAA	10.20	13.32	E12q	CVSO 109/GQ Lupi/EX Lupi
4026.19	He I	2.9e+06	AAA	20.96	24.04	E15q/E12q	CVSO 109/GQ Lupi
4100.74	Fe I	2.9e+04	A	0.86	3.88		GQ Lupi
4101.71	H I	2.9e+06	AAA	10.20	13.22	Z20q/Z20o/E12q	CVSO 109/GQ Lupi/EX Lupi
4178.86	Fe II	1.7e+05	C	2.58	5.55	Z20q/E15q/Z20o/E12q	CVSO 109
4226.34*	Fe I	4.3e+06	D+	2.85	5.78	A17o	EX Lupi
4226.73*	Ca I	2.2e+08	B+	0.00	2.93	Z20q/E15q/E12q	EX Lupi
4233.17	Fe II	7.2e+05	C+	2.58	5.51	E12o/Z20q/E15q/Z20o/E12q/A17o	EX Lupi
4340.47	H I	2.5e+06	AAA	10.20	13.05	Z20q/Z20o/E12q	CVSO 109/GQ Lupi/EX Lupi
4416.83	Fe II	2.1e+05	D	2.78	5.58	E15q	EX Lupi
4471.48	He I	6.8e+05	AAA	20.96	23.74	E15q	CVSO 109/GQ Lupi/EX Lupi
4481.13	Mg II	2.3e+08	A	8.86	11.63		EX Lupi
4508.29	Fe II	7.0e+05	D	2.86	5.60	Z20q/E15q/Z20o/E12q	EX Lupi
4549.47	Fe II	1.0e+06	C+	2.83	5.55	E12o/Z20q/E15q/Z20o/E12q/A17o	EX Lupi
4583.83	Fe II	7.2e+05	C+	2.81	5.51	Z20q/Z20o/E12q	EX Lupi
4685.80	He II	2.2e+08	AA	48.37	51.02	E12q	GQ Lupi/EX Lupi
4861.28	H I	1.7e+07	AAA	10.20	12.75	E12o/E12q/A17o/Z20q/Z20o	CVSO 109/GQ Lupi/EX Lupi
4921.93	He I	2.0e+07	AAA	21.22	23.74	E15q/E12q	EX Lupi
4923.92	Fe II	4.3e+06	C	2.89	5.41	Z20q/E15q/Z20o/E12q/A17o	GQ Lupi/EX Lupi
5015.68*	He I	1.3e+07	AAA	20.62	23.09	E15q/E12q	GQ Lupi/EX Lupi
5015.75*	Fe II	6.2e+07	B+	10.35	12.82		GQ Lupi/EX Lupi
5016.61	V II	2.6e+06	C	5.54	8.01		EX Lupi

Continued on next page

Table D1: List of lines identified in EX Lupi, CVSO 109, GQ Lupi A. Previous ID column corresponds to lines identified in our previous work. o: outburst, q: quiescence. E12,E15: EX Lupi (Sicilia-Aguilar et al. 2012, 2015), A17: ASASSN-13db (Sicilia-Aguilar et al. 2017), Z20: ZCma (Sicilia-Aguilar et al. 2020a). Wavelengths marked by * indicate possible blends or multiple matches to the identified line. Acc denotes the accuracy for each transition strength from the NIST database, ranging from $\leq 0.3\%$ for AAA to $> 50\%$ for E.

λ (Å)	Element	Aki [s]	Acc	Ei [eV]	Ek [eV]	Previous ID	Star
5018.43	Fe II	2.0e+06	D+	2.89	5.36	E12o/Z20q/E15q/Z20o/E12q/A17o	CVSO 109/GQ Lupi/EX Lupi
5167.32*	Mg I	1.1e+07	B+	2.71	5.11	E12q/A17o	EX Lupi
5167.48*	Fe I	2.7e+06	B+	1.48	3.88	E12q	EX Lupi
5169.03	Fe II	4.2e+06	C	2.89	5.29	E15q/Z20o/E12q	CVSO 109/GQ Lupi/EX Lupi
5172.68	Mg I	3.3e+07	B	2.71	5.11	Z20q/E15q/Z20o/E12q/A17o	EX Lupi
5183.49*	Fe II	1.8e+06	D+	10.43	12.82		EX Lupi
5183.60*	Mg I	5.6e+07	B	2.72	5.11	Z20q/E15q/Z20o/E12q/A17o	EX Lupi
5185.91	Ti II	1.0e+06	B+	1.89	4.28	E15q/E12q	EX Lupi
5197.58	Fe II	5.5e+05	C	3.23	5.62	Z20q/E15q/Z20o/E12q	EX Lupi
5234.62	Fe II	2.5e+05	D+	3.22	5.59	E12o/Z20q/E15q/Z20o	EX Lupi
5269.54	Fe I	1.3e+06	A	0.86	3.21	Z20q/E15q/Z20o/E12q	EX Lupi
5276.00	Fe II	3.8e+05	C	3.20	5.55	E12o/Z20q/Z20o/E12q	EX Lupi
5284.11	Fe II	1.9e+04	E	2.89	5.24	E12q/E12o/Z20q/E15q/Z20o	EX Lupi
5316.62	Fe II	3.9e+05	C	3.15	5.48	E12o/Z20q/E15q/Z20o/E12q/A17o	EX Lupi
5362.86	Fe II	1.5e+07	B+	10.50	12.81	E12q	EX Lupi
5534.85	Fe II	3.0e+04	E	3.24	5.48	E12o/Z20q/E15q/Z20o/E12q/A17o	EX Lupi
5577.34	O I	1.3e+00	B+	1.97	4.19	Z20q/Z20o	GQ Lupi
5875.62	He I	1.8e+07	AAA	20.96	23.07	E12o/E12q/Z20q/E15q/Z20o	CVSO 109/GQ Lupi/EX Lupi
5889.95	Na I	6.2e+07	AA	0.00	2.10	Z20q/Z20o/E12q/A17o	EX Lupi
6147.73	Fe II	1.3e+05	E	3.89	5.90	E15q	EX Lupi
6247.56	Fe II	1.6e+05	D	3.89	5.88	E12o/Z20q/E15q/Z20o/E12q/A17o	EX Lupi
6300.30	O I	5.6e-03	C+	0.00	1.97	Z20q/Z20o	CVSO 109/GQ Lupi/EX Lupi
6347.10	Si II	5.8e+07	B+	8.12	10.07	E12o/E15q/Z20o/E12q/A17o	EX Lupi
6363.78	O I	1.6e-03	C+	0.02	1.97	Z20q/Z20o	EX Lupi
6371.36	Si II	6.8e+07	C+	8.12	10.07	E12o/E15q/E12q/A17o	EX Lupi
6456.38	Fe II	1.7e+05	D	3.90	5.82	E12o/Z20q/E15q/Z20o/E12q/A17o	EX Lupi
6562.71	H I	5.4e+07	AAA	10.20	12.09		CVSO 109/GQ Lupi/EX Lupi
6677.98	Fe I	6.3e+05	B	2.69	4.55		GQ Lupi
6678.15	He I	6.4e+07	AAA	21.22	23.07	E12o/Z20q/E15q/Z20o/E12q	CVSO 109/GQ Lupi/EX Lupi
7065.19	He I	1.5e+07	AAA	20.96	22.72	E12o/E15q/E12q	GQ Lupi/EX Lupi
7771.94	O I	3.7e+07	A	9.15	10.74	E15q/Z20o/E12q	EX Lupi
8446.25	O I	3.2e+07	B	9.52	10.99	E15q/Z20o/E12q/A17o	GQ Lupi/EX Lupi
8498.02	Ca II	1.1e+06	C	1.69	3.15	E12o/Z20o/E12q/A17o	CVSO 109/GQ Lupi/EX Lupi
8499.62	Fe II	2.3e+07	B+	9.76	11.22		CVSO 109
8542.09	Ca II	9.9e+06	C	1.70	3.15	Z20o/E12q/A17o	CVSO 109/GQ Lupi/EX Lupi
8545.38	H I	6.5e+03	AAA	12.09	13.54		CVSO 109
8662.14	Ca II	1.1e+07	C	1.69	3.12	E12o/Z20o/E12q/A17o	CVSO 109/GQ Lupi/EX Lupi
8665.02	H I	1.3e+04	AAA	12.09	13.52		CVSO 109
8862.78	H I	3.2e+04	AAA	12.09	13.49	Z20o	GQ Lupi
8886.18	Fe II	9.0e+05	D+	11.26	12.65		GQ Lupi
9014.91	H I	5.2e+04	AAA	12.09	13.46	A17o	GQ Lupi
9015.30	H I	5.2e+04	AAA	12.09	13.46	Z20o	GQ Lupi
9229.01	H I	8.9e+04	AAA	12.09	13.43		GQ Lupi
9440.44	Fe II	3.4e+05	E	12.38	13.69		CVSO 109
10049.37	H I	3.4e+05	AAA	12.09	13.32		CVSO 109/GQ Lupi
10826.48	Fe II	7.2e+05	C+	9.70	10.85		GQ Lupi
10830.25	He I	1.0e+07	AAA	19.82	20.96		CVSO 109/GQ Lupi
10937.99	H I	9.6e+05	AAA	12.09	13.22		CVSO 109/GQ Lupi
12818.07	H I	2.2e+06	AAA	12.09	13.05		CVSO 109/GQ Lupi

APPENDIX E: RADIAL VELOCITY VS MJD FITS FOR EX LUPUI

Included in the supplementary material of the article.

Table E1. Examples of best fit to the line radial velocity. As period we list the maximum of the GLS periodogram excluding aliases, and we also provide the false-alarm-probability (FAP, assuming a white noise model). * The phase offset is calculated using the period for the He II line and the zero point MJD 54309.1147. The amplitude is obtained by fitting Equation 5 to the line velocities. Objects marked as having quasi-periods tend to show multiple low-significance lines around the quasi-period value. Note that wavelengths $>6700\text{\AA}$ are not covered by HARPS.

Species/ λ (\AA)	Amplitude (km/s)	Offset (km/s)	Phase* (deg)	Period (d)	FAP	# of epochs	Notes
HeII 4686	2.5 ± 0.3	4.5 ± 0.2	-38 ± 8	7.41684	2e-8	126	
HeI 4471	1.1 ± 0.2	4.2 ± 0.1	6 ± 10	7.41710	3e-4	112	
HeI 4713	1.8 ± 0.3	4.9 ± 0.2	20 ± 20	6.45204	0.002	65	Very noisy, quasiperiods 6-8 d
HeI 4922	0.8 ± 2	4.0 ± 0.1	-20 ± 20	8.59905	0.008	63	Very noisy line
HeI 5016	1.0 ± 0.1	0.37 ± 0.08	-6 ± 6	7.41481	5e-12	120	
HeI 7065	2.0 ± 0.2	4.2 ± 0.2	33 ± 8	7.41299	3e-6	72	Near tellurics
FeII 4179	1.5 ± 0.2	-0.8 ± 0.1	7 ± 8	6.98646	6e-7	90	Quasiperiod
FeII 4233	1.0 ± 0.1	-0.77 ± 0.09	-13 ± 7	7.41527	6e-9	103	
FeII 4523	1.1 ± 0.2	-0.8 ± 0.1	20 ± 10	6.99165	2e-5	89	Quasiperiods 7-8d
FeII 4549	1.3 ± 0.2	1.4 ± 0.1	-41 ± 9	7.41811	3e-7	117	
FeII 4584	1.1 ± 0.2	-0.1 ± 0.1	11 ± 9	7.41373	1e-4	88	
FeII 4923	1.0 ± 0.1	0.7 ± 0.1	-4 ± 9	6.75582	2e-8	132	Near HeI line
FeII 5018	1.0 ± 0.1	0.94 ± 0.09	10 ± 10	6.11926	3e-7	129	Quasiperiod 6-8d
FeII 5198	1.1 ± 0.1	-0.6 ± 0.1	11 ± 8	7.41787	5e-7	82	
FeII 5235	1.6 ± 0.2	0.4 ± 0.1	1 ± 6	7.41507	1e-12	121	
FeII 5317	1.5 ± 0.2	1.4 ± 0.1	-18 ± 6	7.41633	7e-13	113	
FeII 5362	1.1 ± 0.2	0.8 ± 0.1	30 ± 10	7.59673	2e-4	63	
FeII 6247	0.8 ± 0.2	-1.0 ± 0.1	-50 ± 20	9.91940	0.04	32	
FeII 6456	1.3 ± 0.2	-0.4 ± 0.2	-30 ± 20	7.59270	0.004	47	
FeI 5269	1.6 ± 0.2	-0.4 ± 0.1	-6 ± 6	7.41557	3e-13	114	
SiII 6347	1.3 ± 0.1	-0.3 ± 0.1	14 ± 6	7.41586	2e-9	96	
MgI 5167	1.5 ± 0.2	2.8 ± 0.1	-24 ± 8	7.41583	7e-9	117	
MgI 5172	1.3 ± 0.2	0.2 ± 0.1	-11 ± 7	7.41380	6e-10	128	
MgI 5184	1.4 ± 0.1	0.01 ± 0.09	4 ± 5	7.41557	5e-15	125	
MgII 4481	2.8 ± 0.6	2.4 ± 0.4	-10 ± 20	6.65702	0.04	59	Quasiperiod 6-8d, little data
CaII 8662	0.37 ± 0.06	0.99 ± 0.04	-110 ± 20	3.10937	2e-4	109	Double spot, half a rotational period?
OI 8446	2.5 ± 0.4	5.3 ± 0.3	40 ± 20	5.940127	6e-4	68	Nearby tellurics

The tables shown here contain the results of fitting the radial velocity vs MJD with the rotational modulation equation (eq. 5) used to derive the position of the line-emitting region for various lines observed in the HARPS, FEROS, and ESPaDOnS spectra of EX Lupi.

Table E2: Results of fitting the radial velocity of strong lines in EX Lupi, following Eq. 5.

Species/ λ (\AA)	MJD interval [d]	Amplitude [km/s]	V_0 [km/s]	Phase [deg]	# of points
CaII 8662	56489.0 - 56550.1	0.8 ± 0.1	1.2 ± 0.1	-90 ± 7	11
FeI 5269	54874.3 - 55058.0	1.8 ± 0.5	-0.2 ± 0.4	12 ± 16	11
"	55257.3 - 55407.1	0.5 ± 0.2	-0.5 ± 0.1	2 ± 17	18
"	55586.4 - 55674.3	0.9 ± 0.3	-0.1 ± 0.2	-52 ± 21	14
"	56704.3 - 56709.4	3.0 ± 0.3	-0.5 ± 0.2	5 ± 4	17
"	56489.0 - 56709.4	2.1 ± 0.3	-0.4 ± 0.3	3 ± 9	26
"	57548.4 - 57563.4	1.8 ± 0.3	-0.5 ± 0.3	-32 ± 14	28
FeII 4233	55257.3 - 55407.1	0.4 ± 0.2	-0.6 ± 0.1	-13 ± 20	16
"	55586.4 - 55674.3	1.0 ± 0.3	-0.2 ± 0.2	-73 ± 20	13
"	56704.3 - 56709.4	3 ± 1	-1.1 ± 0.7	-12 ± 15	15
"	56489.0 - 56709.4	2.0 ± 0.8	-1.0 ± 0.5	-16 ± 21	20
"	57548.4 - 57563.4	1.1 ± 0.2	-1.0 ± 0.2	-47 ± 15	31
FeII 4549	54874.3 - 55058.0	0.6 ± 0.2	1.3 ± 0.2	-35 ± 23	10
"	55257.3 - 55407.1	0.2 ± 0.3	2.2 ± 0.2	-72 ± 73	19
"	55586.4 - 55674.3	1.6 ± 0.3	2.6 ± 0.2	-63 ± 12	14
"	56111.0 - 56121.1	1.9 ± 0.6	1.4 ± 0.5	-30 ± 19	10
"	56704.3 - 56709.4	5 ± 1	0.6 ± 0.8	-40 ± 12	15
"	56489.0 - 56709.4	3.5 ± 0.9	0.9 ± 0.6	-56 ± 14	24
"	57548.4 - 57563.4	1.7 ± 0.2	0.6 ± 0.2	-35 ± 12	31
FeII 4924	54874.3 - 55058.0	1.2 ± 0.4	0.2 ± 0.3	25 ± 18	11

Continued on next page

Table E2: Results of fitting the radial velocity of strong lines in EX Lupi, following Eq. 5.

Species/ λ (Å)	MJD interval [d]	Amplitude [km/s]	V_0 [km/s]	Phase [deg]	# of points
"	55257.3 - 55407.1	0.1±0.2	0.5±0.1	-165±118	18
"	55587.4 - 55674.3	0.9±0.3	0.4±0.2	-60±19	13
"	56111.0 - 56121.1	1.9±0.5	0.5±0.4	27±17	10
"	56489.0 - 56550.1	2.1±0.7	0.6±0.4	-65±16	11
"	56704.3 - 56709.4	2.2±0.2	0.3±0.2	19±6	17
"	56489.0 - 56709.4	1.6±0.3	0.3±0.2	5±12	28
"	57548.4 - 57563.4	1.2±0.2	1.2±0.2	-16±11	42
"	58634.4 - 58643.5	5±2	3±5	90±60	12
FeII 5018	54874.3 - 55058.0	0.6±0.3	0.5±0.2	88±31	11
"	55257.3 - 55407.1	0.4±0.2	0.4±0.1	-114±32	19
"	55586.4 - 55674.3	0.9±0.3	0.6±0.2	-76±22	14
"	56111.0 - 56121.1	2.0±0.8	0.3±0.6	1±26	10
"	56489.0 - 56550.1	1.9±0.7	0.8±0.5	-60±19	11
"	56704.3 - 56709.4	2.1±0.2	1.3±0.2	24±7	15
"	56489.0 - 56709.4	1.7±0.4	1.0±0.3	7±14	26
"	57548.4 - 57563.4	1.2±0.3	1.6±0.2	-16±14	43
"	58634.4 - 58643.5	8.7±4.8	0.4±5.4	119±28	10
FeII 5235	55257.3 - 55407.1	0.4±0.2	-0.1±0.1	16±25	18
"	55586.4 - 55674.3	0.8±0.4	0.1±0.3	-41±27	14
"	56489.0 - 56550.1	1.2±0.4	0.6±0.4	-9±31	10
"	56704.3 - 56709.4	2.4±0.3	-0.1±0.2	21±7	16
"	56489.0 - 56709.4	1.9±0.3	0.2±0.2	22±9	26
"	57548.4 - 57563.4	1.7±0.3	1.0±0.2	-17±11	35
FeII 5317	55257.3 - 55407.1	0.5±0.3	2.0±0.2	-7±30	19
"	55586.4 - 55674.3	1.2±0.2	2.2±0.2	-49±11	14
"	56704.3 - 56709.4	2.8±0.3	1.3±0.2	-3±6	16
"	56489.2 - 56709.4	1.8±0.5	1.2±0.3	-14±14	23
"	57548.4 - 57563.4	1.9±0.1	0.9±0.1	-35±6	34
HeI 4471	54874.3 - 55058.0	1.8±0.4	4.0±0.2	-12±10	10
"	55257.3 - 55407.1	0.4±0.4	5.1±0.3	71±61	17
"	55586.4 - 55674.3	1.0±0.3	5.9±0.2	-36±15	14
"	56111.0 - 56121.1	2.5±0.7	4.0±0.6	-7±19	10
"	56704.3 - 56709.4	2.8±0.3	4.6±0.2	-3±6	14
"	56489.0 - 56709.4	1.7±0.4	4.4±0.3	6±16	21
"	57548.4 - 57563.4	1.3±0.2	3.0±0.1	-9±9	29
HeI 5016	55257.3 - 55407.1	0.5±0.2	0.4±0.2	2±23	17
"	55586.4 - 55674.3	0.9±0.2	0.6±0.2	-28±14	13
"	56111.0 - 56121.1	2.0±0.2	-0.2±0.2	9±7	10
"	56704.3 - 56709.4	2.2±0.2	-0.2±0.1	-0±4	16
"	56489.0 - 56709.4	1.7±0.3	-0.3±0.2	3±8	19
"	57548.4 - 57563.4	0.8±0.1	0.7±0.1	-20±7	41
HeII 4686	55257.3 - 55407.1	1.7±0.6	5.6±0.5	-18±21	15
"	55586.4 - 55674.3	3.1±0.5	7.3±0.4	-45±9	13
"	56489.0 - 56550.1	0.9±1.0	5.4±0.6	-68±57	10
"	56704.3 - 56709.4	4.4±0.6	4.5±0.4	-36±6	14
"	56489.0 - 56709.4	2.3±0.6	4.9±0.4	-41±15	24
"	57548.4 - 57563.4	2.9±0.3	2.7±0.2	-17±6	38
"	58634.4 - 58643.5	1.5±1.1	2.3±2.5	-91±110	10
MgI 5167	55257.3 - 55407.1	0.2±0.2	3.0±0.2	-103±75	18
"	55586.4 - 55674.3	0.9±0.3	3.3±0.2	-59±18	14
"	56489.0 - 56709.4	1.6±0.4	2.2±0.4	-63±19	17
"	57548.4 - 57563.4	2.2±0.2	1.8±0.2	-63±8	28
MgI 5173	54874.3 - 55058.0	0.8±0.3	-0.4±0.3	89±27	10
"	55257.3 - 55407.1	0.9±0.4	-0.3±0.3	15±25	19
"	55586.4 - 55674.3	0.8±0.3	0.4±0.2	-44±21	14

Continued on next page

Table E2: Results of fitting the radial velocity of strong lines in EX Lupi, following Eq. 5.

Species/ λ (Å)	MJD interval [d]	Amplitude [km/s]	V_0 [km/s]	Phase [deg]	# of points
"	56489.0 - 56550.1	2.3 ± 0.7	-0.0 ± 0.4	-70 ± 13	11
"	56704.3 - 56709.4	2.5 ± 0.4	-0.1 ± 0.2	3 ± 8	16
"	56489.0 - 56709.4	1.8 ± 0.4	-0.2 ± 0.3	-10 ± 13	27
"	57548.4 - 57563.4	1.7 ± 0.3	-0.6 ± 0.2	-39 ± 11	38
MgI 5184	54874.3 - 55058.0	1.4 ± 0.3	0.0 ± 0.2	47 ± 14	10
"	55257.3 - 55407.1	0.4 ± 0.2	0.1 ± 0.1	9 ± 25	19
"	55586.4 - 55674.3	1.0 ± 0.3	0.4 ± 0.2	-31 ± 15	14
"	56111.0 - 56121.1	2.0 ± 0.6	0.1 ± 0.4	2 ± 19	10
"	56489.0 - 56550.0	2.4 ± 1.0	0.3 ± 0.6	-61 ± 21	10
"	56704.3 - 56709.4	2.5 ± 0.2	0.2 ± 0.1	12 ± 4	16
"	56489.0 - 56709.4	1.9 ± 0.4	0.2 ± 0.3	2 ± 12	26
"	57548.4 - 57563.4	1.6 ± 0.2	-0.4 ± 0.2	-14 ± 9	36
SiII 6347	55257.3 - 55407.1	0.7 ± 0.2	-0.1 ± 0.1	18 ± 16	19
"	55586.4 - 55674.3	1.1 ± 0.3	0.1 ± 0.2	-26 ± 16	14
"	56111.0 - 56121.1	1.6 ± 0.4	0.1 ± 0.3	35 ± 17	10
"	56704.3 - 56709.4	2.7 ± 0.3	-0.8 ± 0.2	14 ± 7	17
"	56489.0 - 56709.4	1.9 ± 0.5	-0.7 ± 0.3	6 ± 15	26
"	57548.4 - 57563.4	2.1 ± 0.5	-0.7 ± 0.3	14 ± 12	14

APPENDIX F: CVSO109 GAUSSIAN FIT PROPERTIES

Included in the supplementary material of the article.

This paper has been typeset from a \LaTeX file prepared by the author.

Table F1. CVSO109 summary of the composite Gaussian fit to the lines possessing a clearly defined emission wing, which could be accurately fitted across the four epochs; and the Ca II IR triplet fitted in the XSHOOTER data. Standard errors for the Gaussian components are indicated.

UTC observation date (Instrument)	Species	λ (air) [Å]	g1_cen [km/s]	g2_cen [km/s]	g1_fwhm [km/s]	g2_fwhm [km/s]	Aki [s]	Ek [eV]
2020-11-26T03:29:49.172_UVES	H I	3750.2	2.1 ± 1.2	-17.1 ± 3.8	45.9 ± 3.7	197.5 ± 11.5	$2.8\text{E}+04$	13.5
2020-11-28T03:36:03.569_XSHOOTER	H I	3750.2	-6.1 ± 0.5	67.3 ± 0.7	59.1 ± 1.4	286.3 ± 1.7	$2.8\text{E}+04$	13.5
2020-11-26T03:29:49.172_UVES	H I	3770.6	1.9 ± 0.5	-8.8 ± 1.5	38.4 ± 1.5	189.3 ± 4.9	$4.4\text{E}+04$	13.5
2020-11-27T03:02:55.805_UVES	H I	3770.6	1.8 ± 0.5	-1.1 ± 1.6	49.7 ± 1.6	230 ± 5.7	$4.4\text{E}+04$	13.5
2020-11-28T03:36:03.569_XSHOOTER	H I	3770.6	-7.7 ± 0.3	71.7 ± 0.6	68.8 ± 0.9	293.7 ± 1.3	$4.4\text{E}+04$	13.5
2020-11-28T03:59:39.410_UVES	H I	3770.6	1 ± 0.5	60 ± 1.3	45.6 ± 1.3	277 ± 3.5	$4.4\text{E}+04$	13.5
2020-11-26T03:29:49.172_UVES	H I	3797.9	-0.8 ± 0.4	-13.6 ± 1.5	56.7 ± 1.3	232.3 ± 5.4	$7.1\text{E}+04$	13.5
2020-11-27T03:02:55.805_UVES	H I	3797.9	0.5 ± 0.4	-7.8 ± 1.5	60.5 ± 1.5	228 ± 5.6	$7.1\text{E}+04$	13.5
2020-11-28T03:36:03.569_XSHOOTER	H I	3797.9	-5.1 ± 0.2	63 ± 0.4	68.2 ± 0.5	295.7 ± 1	$7.1\text{E}+04$	13.5
2020-11-28T03:59:39.410_UVES	H I	3797.9	-0.7 ± 0.4	57.5 ± 1	50.5 ± 1	267.5 ± 2.6	$7.1\text{E}+04$	13.5
2020-11-26T03:29:49.172_UVES	H I	3835.3	2.6 ± 0.5	-2.4 ± 1.6	46.8 ± 1.4	201.4 ± 5.6	$1.2\text{E}+05$	13.4
2020-11-27T03:02:55.805_UVES	H I	3835.3	2.8 ± 0.4	1.2 ± 1.4	50.2 ± 1.2	209.4 ± 5.1	$1.2\text{E}+05$	13.4
2020-11-28T03:36:03.569_XSHOOTER	H I	3835.3	-2.2 ± 0.2	56.3 ± 0.5	71.3 ± 0.7	279.5 ± 1.3	$1.2\text{E}+05$	13.4
2020-11-28T03:59:39.410_UVES	H I	3835.3	3.3 ± 0.4	52.4 ± 1.2	50 ± 1.1	264.5 ± 3.3	$1.2\text{E}+05$	13.4
2020-11-26T03:29:49.172_UVES	H I	3889.1	-7 ± 0.2	-15.4 ± 1.2	68.4 ± 0.8	248.1 ± 4.9	$2.2\text{E}+05$	13.4
2020-11-27T03:02:55.805_UVES	H I	3889.1	-5.6 ± 0.3	-11.2 ± 1	66.2 ± 1	218 ± 4.1	$2.2\text{E}+05$	13.4
2020-11-28T03:36:03.569_XSHOOTER	H I	3889.1	-9.4 ± 0.1	37.8 ± 0.2	78 ± 0.2	276.1 ± 0.6	$2.2\text{E}+05$	13.4
2020-11-28T03:59:39.410_UVES	H I	3889.1	-5.9 ± 0.3	33.8 ± 0.9	64.1 ± 0.8	260.9 ± 2.6	$2.2\text{E}+05$	13.4
2020-11-26T03:29:49.172_UVES	H I	4101.7	2.6 ± 0.2	-7.7 ± 0.7	59.2 ± 0.6	205.7 ± 2.5	$2.9\text{E}+06$	13.2
2020-11-27T03:02:55.805_UVES	H I	4101.7	2.6 ± 0.2	0.9 ± 0.6	55.2 ± 0.7	194.8 ± 2.4	$2.9\text{E}+06$	13.2
2020-11-28T03:36:03.569_XSHOOTER	H I	4101.7	0 ± 0.1	39.4 ± 0.3	73.7 ± 0.4	248.3 ± 0.7	$2.9\text{E}+06$	13.2
2020-11-28T03:59:39.410_UVES	H I	4101.7	3.4 ± 0.2	34.9 ± 0.5	53.3 ± 0.5	234.2 ± 1.5	$2.9\text{E}+06$	13.2
2020-11-26T03:29:49.172_UVES	H I	4340.5	0.2 ± 0.2	-7.6 ± 0.8	63.9 ± 0.6	217 ± 3	$2.5\text{E}+06$	13.1
2020-11-27T03:02:55.805_UVES	H I	4340.5	0.8 ± 0.2	0.7 ± 0.6	59 ± 0.7	198.8 ± 2.5	$2.5\text{E}+06$	13.1
2020-11-28T03:36:03.569_XSHOOTER	H I	4340.5	-3.2 ± 0.1	35.7 ± 0.2	73 ± 0.3	232.9 ± 0.6	$2.5\text{E}+06$	13.1
2020-11-28T03:59:39.410_UVES	H I	4340.5	0.8 ± 0.2	34.1 ± 0.5	57.6 ± 0.5	230 ± 1.4	$2.5\text{E}+06$	13.1
2020-11-26T03:29:45.199_UVES	H I	4861.4	-1.2 ± 0.2	-15 ± 1.1	71.3 ± 0.6	256.6 ± 3.9	$2.1\text{E}+07$	12.7
2020-11-27T03:02:45.220_UVES	H I	4861.4	-0.1 ± 0.2	-0.8 ± 0.7	64.8 ± 0.8	200.1 ± 3.1	$2.1\text{E}+07$	12.7
2020-11-28T03:36:03.569_XSHOOTER	H I	4861.4	-5.4 ± 0.1	30.7 ± 0.3	83.8 ± 0.4	244.6 ± 0.7	$2.1\text{E}+07$	12.7
2020-11-28T03:59:35.437_UVES	H I	4861.4	-1.7 ± 0.2	33.4 ± 0.5	69.1 ± 0.6	237.2 ± 1.3	$2.1\text{E}+07$	12.7
2020-11-26T03:29:45.199_UVES	H I	6562.8	-3.4 ± 0.2	2.7 ± 0.9	96.2 ± 1	220.5 ± 4.8	$4.4\text{E}+07$	12.1
2020-11-27T03:02:45.220_UVES	H I	6562.8	-0.6 ± 0.6	0 ± 1.9	70 ± 2.6	175.3 ± 3.5	$4.4\text{E}+07$	12.1
2020-11-28T03:36:08.759_XSHOOTER	H I	6562.8	-3.5 ± 0.1	23.1 ± 0.4	122.1 ± 0.5	252.3 ± 1.4	$4.4\text{E}+07$	12.1
2020-11-28T03:59:35.437_UVES	H I	6562.8	-6.2 ± 0.8	12.9 ± 2	61.9 ± 2.6	242.2 ± 7	$4.4\text{E}+07$	12.1
2020-11-26T03:29:49.172_UVES	Ca II	3933.7	-1.9 ± 0.1	1.1 ± 0.2	16.2 ± 0.3	45.5 ± 0.8	$1.5\text{E}+08$	3.2
2020-11-27T03:02:55.805_UVES	Ca II	3933.7	-1.3 ± 0.1	2.1 ± 0.3	16.5 ± 0.3	48.5 ± 0.9	$1.5\text{E}+08$	3.2
2020-11-28T03:36:03.569_XSHOOTER	Ca II	3933.7	-3.3 ± 0.1	76.7 ± 0.2	62.1 ± 0.2	223.5 ± 0.4	$1.5\text{E}+08$	3.2
2020-11-28T03:59:39.410_UVES	Ca II	3933.7	-0.5 ± 0.1	65.6 ± 0.8	26.6 ± 0.3	217 ± 2.1	$1.5\text{E}+08$	3.2
2020-11-28T03:36:08.759_XSHOOTER	Ca II	8498.0	3 ± 0.2	113.9 ± 1.2	23.4 ± 0.4	164.2 ± 3.4	$1.1\text{E}+06$	3.2
2020-11-28T03:36:08.759_XSHOOTER	Ca II	8542.1	3 ± 0.2	110.9 ± 1.2	28.6 ± 0.5	162 ± 3.5	$9.9\text{E}+06$	3.2
2020-11-28T03:36:08.759_XSHOOTER	Ca II	8662.1	3.4 ± 0.2	118.9 ± 1.1	23.5 ± 0.4	166.7 ± 3.1	$1.1\text{E}+07$	3.1